
PDEBENCH: An Extensive Benchmark for Scientific Machine Learning

Makoto Takamoto*
NEC Labs Europe

Timothy Praditia†
University of Stuttgart

Raphael Leiteritz
University of Stuttgart

Dan MacKinlay
CSIRO's Data61

Francesco Alesiani
NEC Labs Europe

Dirk Pflüger
University of Stuttgart

Mathias Niepert
University of Stuttgart

Abstract

Machine learning-based modeling of physical systems has experienced increased interest in recent years. Despite some impressive progress, there is still a lack of benchmarks for Scientific ML that are easy to use but still challenging and representative of a wide range of problems. We introduce PDEBENCH, a benchmark suite of time-dependent simulation tasks based on Partial Differential Equations (PDEs). PDEBENCH comprises both code and data to benchmark the performance of novel machine learning models against both classical numerical simulations and machine learning baselines. Our proposed set of benchmark problems contribute the following unique features: (1) A much wider range of PDEs compared to existing benchmarks, ranging from relatively common examples to more realistic and difficult problems; (2) much larger ready-to-use datasets compared to prior work, comprising multiple simulation runs across a larger number of initial and boundary conditions and PDE parameters; (3) more extensible source codes with user-friendly APIs for data generation and baseline results with popular machine learning models (FNO, U-Net, PINN, Gradient-Based Inverse Method). PDEBENCH allows researchers to extend the benchmark freely for their own purposes using a standardized API and to compare the performance of new models to existing baseline methods. We also propose new evaluation metrics with the aim to provide a more holistic understanding of learning methods in the context of Scientific ML. With those metrics we identify tasks which are challenging for recent ML methods and propose these tasks as future challenges for the community. The code is available at <https://github.com/pdebench/PDEBench>.

1 Motivation

In the emergent area of *Scientific Machine Learning* (or *machine learning for physical sciences or data-driven science*), recent progress has broadened the scope of traditional machine learning (ML) methods to include the time-evolution of physical systems. Within this field, rapid progress has been made in the use of neural networks to make predictions using functional observations over continuous domains [8, 46] or with challenging constraints and with physically-motivated conservation laws [34, 61, 47]. These neural networks provide an approach to solving PDEs complementing traditional numerical solvers. For instance, data-driven ML methods are useful when observations are noisy or

*E-mail: Makoto.Takamoto@neclab.eu

†E-mail: timothy.praditia@iws.uni-stuttgart.de

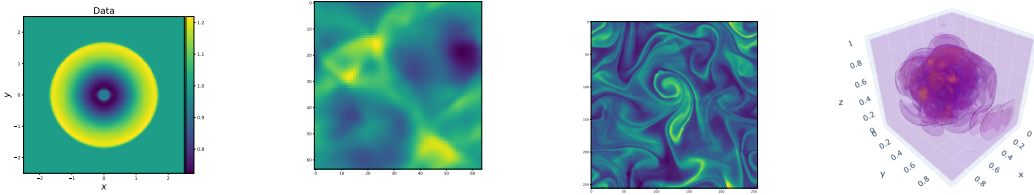


Figure 1: PDEBENCH provides multiple non-trivial challenges from the Sciences to benchmark current and future ML methods, including wave propagation and turbulent flow in 2D and 3D

the underlying physical model is not fully known or defined [11]. Moreover, neural models have the advantage of being continuously differentiable in their inputs, a useful property in several applications. In physical system design [1], for instance, the models are themselves physical objects and thus not analytically differentiable. Similarly, in many fields such as hydrology [14], benchmark physical simulation models exist but the forward simulation models non-differentiable black boxes. This complicates optimisation, control, sensitivity analysis, and solving inverse inference problems. While complex methods such as Bayesian optimisation [38, 50, 42] or reduced order modelling [16] are in part an attempt to circumvent this lack of differentiability, gradients for neural networks are readily available and efficient.

For classical ML applications such as image classification, time series prediction or text mining, various popular benchmarks exist, and evaluations using these benchmarks provides a standardised means of testing the effectiveness and efficiency of ML models. As yet, a widely accessible, practically simple, and statistically challenging benchmark with ready-to-use datasets to compare methods in Scientific ML is missing. While some progress towards reference benchmarks has been made in recent years (see section 2), we aim to provide a benchmark that is more comprehensive with respect to the PDEs covered and which enables more diverse methods for evaluating the efficiency and accuracy of the ML method. The problems span a range of governing equations as well as different assumptions and conditions; see Figure 1 for a visual teaser. Data may be generated by executing code through a common interface, or by downloading high-fidelity datasets of simulations. All code is released under a permissive open source license, facilitating re-use and extension. We also propose an API to ease the implementation and evaluation of new methods, provide recent competitive baseline methods such as FNOs and autoregressive models based on the U-Net, and a set of pre-computed performance metrics for these algorithms. We may thus compare their predictions against the “ground truth” provided by baseline simulators used to generate the data.

As in other machine learning application domains, benchmarks in Scientific ML may serve as a source of readily-available training data for algorithm development and testing without the overhead of generating data *de novo*. In these emulation tasks, the training/test data is notionally unlimited, since more data may always be generated by running a simulator. However, in practice, producing such datasets can have an extremely high burden in compute time, storage and in access to the specialised skills needed to produce them. PDEBENCH also addresses the need for quick, off-the-shelf training data, bypassing these barriers while providing an easy on-ramp to be extended.

In this work, we propose a versatile benchmark suite for Scientific ML (a) providing diverse data sets with distinct properties based on 11 well-known time-dependent and time-independent PDEs, (b) covering both “classical” forward learning problems and inverse settings, (c) all accessible via a uniform interface to read/store data across several applications, (d) extensible, (e) with results for popular state-of-the-art ML models (FNO, U-Net, PINN) for (f) a set of metrics that are better-suited for Scientific ML, (g) with both data to download and code to generate more data, and (h) pre-trained models to compare against. The inverse problem scenarios comprise initial and boundary conditions and PDE parameters (e.g. viscosity). Each data set has a sufficiently large number of samples for training and test, for a variety of parameter values, with a resolution high enough to capture local dynamics. As an additional note, our goal is not to provide a complete benchmark that includes all possible combinations of inference tasks on all known experiments, but rather to ease the task for subsequent researchers to benchmark their favoured methods. Part of our goal here is to invite other researchers to fill in the gaps for themselves by leveraging our ready-to-run models.

To evaluate ML methods for scientific problems, we consider several metrics that go beyond the standard RMSE and include properties of the underlying physics. The initial experimental results we obtained using PDEBENCH confirm the need for comprehensive Scientific ML benchmarks: There is no one-size-fits-all model and there is plenty of room for new ML developments. The results show that the standard error measure in ML, the RMSE on test data, is not a good proxy for evaluating ML models, in particular in turbulent and non-smooth regimes where it fails to capture small spatial scale changes. We furthermore cover an application where a parameter of the underlying PDE heavily influences the difficulty of the problem for ML baselines. We also observe unexpected experimental results for the generalization behavior of auto-regressive training, which seems to be more challenging in the scientific realm. In the remainder of the paper, we first address related work, introduce PDEBENCH and the underlying design choices, and discuss results for a few selected experiments.

2 Related Work

PDE benchmarking has particular challenges. Unlike many classic datasets, PDE datasets can be large on a gigabyte or terabyte scale and still contain only few data points. And unlike monolithic benchmark datasets such as ImageNet, the datasets for each PDE approximation task are specific to that task. Each set of governing equations or experiment design assumptions leads to a distinct dataset of PDE samples. Recent works in PDEs have attempted to produce standardised datasets covering well-known challenges [44, 19, 51]. [19] targets non-ML uses. [51] is specialised for particular classes of equations. Of these, the excellent work of [44] is most closely related, but with only four physical systems, it still lacks sufficient scale and diversity of data to challenge emerging ML algorithms. We expand the range of benchmarks in this domain by providing a larger, more diverse problem selection and scale than these previous attempts (11 PDEs with different parametrizations leading to 35 datasets). We additionally consider inverse problems for PDEs [53, 56], with the goal to identify unobserved latent parameters using ML. This has not been covered by benchmarks so far, despite its increasing importance in the community. Furthermore, most work in this scope considers classical statistical error measures such as the RMSE over the whole domain and at most PDE-motivated variants such as the RMSE of the gradient [44]. Measures based on properties of the underlying physical systems, as studied in this work, are lacking.

An overview and taxonomy of Scientific ML developments can be found in [28, 6]. For developing our baselines, we focus on using neural network models to approximate the outputs of some *ground truth* PDE solver, given data generated by that solver, which itself aims to directly implement the numerical solution of a given partial differential equation. A range of methods aim to solve problems fitting this description, reviewed in [22]. Methods include Physics-informed neural networks (PINNs) [47], Neural operators (NOs) [32, 26], treating ResNet as a PDE approximant [49], custom architectures for specific problems such as TFNet for turbulent fluid flows [61], and generic image-to-image regression models such as the U-Net [48]. These approaches each have different assumptions, domains of applicability, and data processing requirements. For a more comprehensive discussion of prior work in Scientific ML we refer the reader to Appendix A.

3 PDEBENCH: A Benchmark for Scientific Machine Learning

In the following we describe the general learning problem addressed with the benchmark, the currently covered PDEs, existing implemented baselines (all developed using PyTorch [45], and PINN specifically using DeepXDE [34]), and the ways in which the benchmark follows FAIR data principles [63].

3.1 General Problem Definition

A solution to a PDE is a vector-valued function $\mathbf{v} : \mathcal{T} \times \mathcal{S} \times \Theta \rightarrow \mathbb{R}^d$ on some spatial domain \mathcal{S} , with temporal index \mathcal{T} , and some possibly function-valued parameter-space Θ . For example in a heat diffusion equation, \mathbf{v} might represent the local temperature $\tau \in \mathbb{R}^1$ of some substrate at some given point $\mathbf{s} \in \mathcal{S}$, at a given moment $t \in \mathcal{T}$, and conditional upon a spatially-varying scalar conductivity field representing an inhomogeneous substrate $\theta : \mathcal{S} \rightarrow \mathbb{R}^+$. The operator mapping from the state of

Table 1: Summary of PDEBENCH’s datasets with their respective number of spatial dimensions N_d , time dependency, spatial resolution N_s , temporal resolution N_t , and number of samples generated.

| PDE | N_d | Time | N_s | N_t | Number of samples |
|------------------------------|-------|------|-----------------------------|-------|-------------------|
| advection | 1 | yes | 1 024 | 200 | 10 000 |
| Burgers’ | 1 | yes | 1 024 | 200 | 10 000 |
| diffusion-reaction | 1 | yes | 1 024 | 200 | 10 000 |
| diffusion-reaction | 2 | yes | 128×128 | 100 | 1000 |
| diffusion-sorption | 1 | yes | 1 024 | 100 | 10 000 |
| compressible Navier-Stokes | 1 | yes | 1 024 | 100 | 10 000 |
| compressible Navier-Stokes | 2 | yes | 512×512 | 21 | 1000 |
| compressible Navier-Stokes | 3 | yes | $128 \times 128 \times 128$ | 21 | 100 |
| incompressible Navier-Stokes | 2 | yes | 256×256 | 1000 | 1000 |
| Darcy flow | 2 | no | 128×128 | – | 10 000 |
| shallow-water | 2 | yes | 128×128 | 100 | 1000 |

the solution at one timestep to the solution one time step later, $\mathfrak{F}_\theta : \mathbf{v}_\theta(t, \cdot) \rightarrow \mathbf{v}_\theta(t + 1, \cdot)$ is referred to as the *forward propagator*.

The objective of Scientific ML is to find some ML-based surrogate, sometimes referred to as an emulator, of this forward propagator by learning an approximation $\widehat{\mathfrak{F}}_\theta \simeq \mathfrak{F}_\theta$. The forward propagator of a PDE is dependent not only on the current state, but also upon both spatial and temporal derivatives of the state field. In practice, temporal derivatives of solutions are often not conveniently encoded by system states at one single time step. Hence, the forward propagator may also depend on multiple previous timesteps of the solution, enabling finite-difference approximations of the temporal derivatives. The discretised forward propagator $\tilde{\mathfrak{F}}_\theta$ then operates on $\ell \geq 1$ consecutive timesteps so that $\tilde{\mathfrak{F}}_\theta : \mathbf{v}_\theta(t - \ell, \cdot), \dots, \mathbf{v}_\theta(t - 1, \cdot) \mapsto \mathbf{v}_\theta(t, \cdot)$, which is abbreviated as $\mathbf{v}_\theta([t - \ell : t - 1], \cdot) := \mathbf{v}_\theta(t - \ell, \cdot), \dots, \mathbf{v}_\theta(t - 1, \cdot)$.

We seek to approximate this discretised operator with an emulator $\widehat{\mathfrak{F}}_\theta \simeq \tilde{\mathfrak{F}}_\theta$ in the sense that predictions the emulator makes should be close to the ground truth simulation given the same inputs, with respect to some measure of cost. We fix a parametric class of models $\{\mathfrak{F}_{\theta, \phi}\}_\phi$. From this class we *learn* a surrogate $\tilde{\mathfrak{F}}_{\theta, \phi}$ from data. In learning, we take a dataset \mathcal{D} comprising discretized PDE solutions conditional on selected parameter values (θ_k) , $\mathcal{D} := \{\mathbf{v}_{\theta_k}^{(k)}([0 : t_{\max}], \cdot) \mid k = 1, \dots, K\}$. Fixing a loss functional L , we aim to find some ϕ achieving a minimal total loss on the training dataset

$$\widehat{\phi} = \operatorname{argmin}_\phi \sum_{t=1}^{t_{\max}} \sum_{k=1}^K L \left(\tilde{\mathfrak{F}}_{\theta_k, \phi} \{ \mathbf{v}_{\theta_k}^{(k)}([t - \ell : t - 1], \cdot) \}, \mathbf{v}_{\theta_k}^{(k)}(t, \cdot) \right). \quad (1)$$

Due to the use of iterative optimization algorithms such as stochastic gradient descent and the non-convex nature of the above optimization problem, we typically obtain local optima. \mathcal{D} is generated by a ground-truth solver designed to simulate the desired dynamics with high precision. In this data we may vary initial conditions, that is, varying $\mathbf{v}_\theta(0, \cdot)$, varying θ , or both.

In addition to the forward problem, we also consider the use of learned surrogate models to approximately solve *inverse problems* [53, 56], where an unknown initial condition $\mathbf{v}_\theta(0, \cdot)$ or unknown parameter θ is chosen to be congruent with some observed outputs $\mathbf{v}_\theta([t : t + \ell], \cdot)$. We follow [32, 35] in using an approximate surrogate approach, taking the forward surrogates as mean predictors for the model. We assume $\mathbf{v}_\theta(t, \cdot) = \tilde{\mathfrak{F}}_{\theta, \phi} \{ \mathbf{v}_\theta([t - \ell : t - 1], \cdot) \} + \epsilon$ for some mean-zero observation noise ϵ , and assuming a prior distribution for the unknown of interest. Other inversion methods can be used in this domain, such as generative adversarial models, [9] or variational autoencoders [54].

3.2 Overview of Datasets and PDEs

The current version of the benchmark provides datasets generated for various PDEs ranging from 1 to 3 dimensional spatial domains. There are both time-dependent and time-independent PDEs. The current datasets are summarized in Table 1; see Figure 1 for a visual teaser. Each sample is generated with different parameters, initial conditions, and boundary conditions. Generalization to different

parameters, varying initial conditions, and proper treatment of complex boundary conditions are still open challenges in Scientific ML [21, 4, 2, 29]. The parameters which are varied to provide several datasets include the advection speed in the advection equation, the forcing term in the Darcy flow, as well as the viscosity in the Burgers' and compressible Navier-Stokes equations all of which can lead to significantly different behaviors of the simulated systems. Additionally, besides the periodic boundary condition that is most commonly used in Scientific ML studies, we also provide datasets generated with the Neumann boundary condition in the 2D diffusion-reaction and shallow-water equations, the Cauchy boundary condition in the diffusion-sorption equation, and the Dirichlet condition in the incompressible Navier-Stokes equation.

We designed this benchmark to represent a diverse set of challenges for emulation algorithms. In particular, we focus on hydromechanical field equations. Following this philosophy, we selected 6 basic and 3 advanced real-world problems. The basic PDEs are stylized, simple models: 1D advection/Burgers/Diffusion-Reaction/Diffusion-Sorption equations, 2D Diffusion-Reaction equation, and 2D DarcyFlow; the advanced and real-world PDEs incorporate features of real-world modeling tasks: Compressible and incompressible Navier-Stokes equations, and shallow-water equations. The PDEs exhibit a variety of behaviors of real-world significance which are known to challenge emulators, such as sharp shock formation dynamics, sensitive dependence on initial conditions, diverse boundary conditions, and spatial heterogeneity. Finding a surrogate model which can approximate these challenging dynamics with high fidelity we argue is a necessary precondition to applying such models in the real world. While some of these have been used in prior work, a publicly available benchmark dataset is, to the best of our knowledge, not available.

In the following we provide a brief introduction and important features of the advanced PDEs. More detailed explanations for all the PDEs are provided in Appendix D.

Compressible Navier-Stokes equations The compressible fluid dynamics equations describe a fluid flow whose expression is given as:

$$\partial_t \rho + \nabla \cdot (\rho \mathbf{v}) = 0, \quad \rho(\partial_t \mathbf{v} + \mathbf{v} \cdot \nabla \mathbf{v}) = -\nabla p + \eta \Delta \mathbf{v} + (\zeta + \eta/3) \nabla(\nabla \cdot \mathbf{v}), \quad (2a)$$

$$\partial_t (\epsilon + \rho v^2/2) + \nabla \cdot [(p + \epsilon + \rho v^2/2) \mathbf{v} - \mathbf{v} \cdot \sigma'] = \mathbf{0}, \quad (2b)$$

where ρ is the mass density, \mathbf{v} is the fluid velocity, p is the gas pressure, ϵ is an internal energy described by the equation of state, σ' is the viscous stress tensor, and η and ζ are shear and bulk viscosity, respectively. This equation can describe more complex phenomena, such as shock wave formation and propagation. It is applied to many real-world problems, such as the aerodynamics around airplane wings and interstellar gas dynamics.

Incompressible Navier-Stokes equations The Navier-Stokes equation is the incompressible version of the compressible fluid dynamics equation, applicable to sub-sonic flows. This equation can model a variety of systems, from hydromechanical systems to weather forecasting or investigating turbulent dynamics.

Shallow-Water Equations The shallow-water equations, derived from the compressible Navier-Stokes equations, present a suitable framework for modeling free-surface flow problems. In 2D, these come in the form of the following system of hyperbolic PDEs,

$$\partial_t h + \nabla h \mathbf{u} = 0, \quad \partial_t h \mathbf{u} + \nabla \left(\mathbf{u}^2 h + \frac{1}{2} g_r h^2 \right) = -g_r h \nabla b, \quad (3a)$$

where $\mathbf{u} = u, v$ being the velocities in the horizontal and vertical direction, h describing the water depth, and b describing a spatially varying bathymetry. $h \mathbf{u}$ can be interpreted as the directional momentum components and g_r describes the gravitational acceleration. The mass and momentum conservation properties even hold across shocks in the solution and thus challenging datasets can be generated. Example applications include the simulation of tsunamis or general flooding events.

3.3 Overview of Metrics

The standard approach of computing the RMSE on test data falls short of capturing important optimization criteria in Scientific ML. A good fit to (often sparse) data is not sufficient if the physics of the underlying problem is severely violated. Physics-informed learning that aims to conserve

```

from pyDaRUS import Dataset
p_id = "doi:10.18419/darus-2986"
dataset = Dataset.from_dataverse_doi(p_id, filedir="data/")

```

Listing 1: Including a benchmark dataset.

physical quantities must therefore be evaluated with appropriate metrics. A global, averaged metric for instance cannot capture small spatial scale changes critical in turbulent regimes. Moreover, a single evaluation metric is not sufficient to compare different methods with respect to their ability to extrapolate to unseen time steps and parameters which are important but underexplored evaluation criteria for ML surrogates. Hence, the proposed benchmark includes several novel metrics which we believe provide a deeper and more holistic understanding of the surrogate’s behavior and which are designed to reflect both the data and physics perspective. The following table summarizes the metrics used; further details can be found in the Appendix B.

| Scope | Acronym | Metric |
|--------------|------------|---|
| Data view | RMSE | root-mean-squared-error |
| | nRMSE | normalized RMSE (ensuring scale independence) |
| | max error | maximum error (local worst case; also proxy for stability of time-stepping) |
| Physics view | cRMSE | RMSE of conserved value (deviation from conserved physical quantity) |
| | bRMSE | RMSE on boundary (whether boundary condition can be learned) |
| | fRMSE low | RMSE in Fourier space, low frequency regime (wavelength dependence) |
| | fRMSE mid | RMSE in Fourier space, medium frequency regime |
| | fRMSE high | RMSE in Fourier space, high frequency regime |

3.4 Existing Baseline Surrogate Models

U-Net U-Net [48] is an auto-encoding neural network architecture used for processing images using multi-resolution convolutional networks with skip layers. U-Net is a black-box machine learning model that propagates information efficiently at different scales. Here, we extended the original implementation, which uses 2D-CNN, to the spatial dimension of the PDEs (i.e. 1D,3D).

Fourier neural operator (FNO) FNO [32] belongs to the family of Neural Operators (NOs), designed to approximate the forward propagator of PDEs. FNO learns a resolution-invariant NO by working in the Fourier space and has shown success in learning challenging PDEs.

Physics-Informed Neural Networks (PINNs) Physics-informed neural networks [47] are methods for solving differential equations using a neural network $u_\theta(t, x)$ to approximate the solution by turning it into a multi-objective optimization problem. The neural network is trained to minimize the PDE residual as well as the error with regard to the boundary and initial conditions. PINNs naturally integrate observational data [30], but require retraining for each new condition.

Gradient-Based Inverse Method Since the surrogate model is fully differentiable, we use its gradient to solve inverse inference by minimizing the prediction loss [7, 40], where a function surface defining the unknown initial conditions [35], is specified through bilinear interpolation.

3.5 Data Format, Benchmark Access, Maintenance, and Extensibility

The benchmark consists of different data files, one for each equation, type of initial condition, and PDE parameter, using the HDF5 [15] binary data format. Each such file contains multiple arrays where each array has the dimensions N, T, X, Y, Z, V with N the number of samples, T the number of time steps, and X, Y, Z the spatial dimensions and V the dimension of the field. Additional information on the data format is provided in the Supplementary Material.

PDEBENCH’s datasets are stored and maintained using DARUS, the University of Stuttgart’s data repository based on the OpenSource Software DataVerse³. DARUS follows the Findable, Accessible, Interoperable and Reusable (FAIR) data principles [63]. All data uploaded to DaRUS gets a DOI as

³ <https://dataverse.org>

```

from pdebench.models.fno.utils import FNODatasetSingle
filename = "data/2D_diff-react_NA_NA"
train_data = FNODatasetSingle(filename)
train_loader = torch.utils.data.DataLoader(train_data)

```

Listing 2: Using the PyTorch data loader.

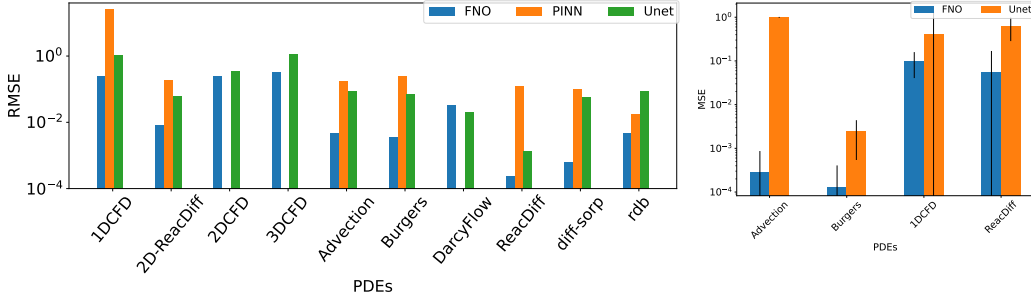


Figure 2: Comparisons of baseline models’ performance for different problems for (a) the forward problem and (b) the inverse problem.

a persistent identifier, a license, and can be described with an extensive set of metadata, organized in metadata blocks. A dedicated team ensures that DARUS is continuously maintained. Through DARUS we provide a permanent DOI (doi:10.18419/darus-2986) [55] for the benchmark data. We also support a straightforward inclusion of the benchmark with a few lines of code. In Listing 1 we demonstrate the way in which the Dataverse [10] platform⁴ supports the integration of pre-generated datasets using a few lines of code. Specifically, we utilize the easy-to-use pyDARUS Python package to access the data. It provides a simple API for both downloading and uploading data as well as providing metadata to the Dataverse platform.

In Listing 2 we show an example leveraging pre-defined classes included in our benchmark code to load specific datasets as PyTorch [45] Dataset classes. Subsequently, these can be used to construct common DataLoader instances for training custom ML models. We utilize the Hydra [64] library simplifying the configuration of both surrogate model training as well as the generation of additional datasets. For the latter, we provide and expose various parameters of the underlying simulations for the end user to tweak. This provides a low barrier of entry for users to try out benchmarking with new experiments or baseline configurations.

4 A Selection of Experiments

In this section, we present a selection of experiments for the PDEBENCH datasets. An exhaustive discussion of all results is beyond the scope of this paper. An extensive set of additional results, tables, and plots can be found in the Appendix.

4.1 Baseline Setups

We trained and tested the baseline emulator models, namely U-Net, FNO, and PINN with the datasets generated with the PDEs described in subsection 3.2. The data was split into training and test data: 90% was for training and 10% for test data. For FNO, we followed the original implementation, hyperparameters, and training protocols. We trained U-Net similarly to FNO, but with the autoregressive methods with the pushforward trick with slight modification to the original implementation [4]. A more comprehensive comparison between different U-Net training methods is presented in subsection 4.3. The PINN baseline is implemented using the open-source DeepXDE [34] library. The training was performed on GeForce RTX 2080 GPUs for 1D/2D cases, and GeForce GTX 3090 for 3D cases. The detailed training protocol and hyper-parameters are provided in Appendix C. Training code and configurations are open and well documented, allowing researchers to easily reproduce or extend these methods.

⁴ https://darus.uni-stuttgart.de/dataverse/sciml_benchmark

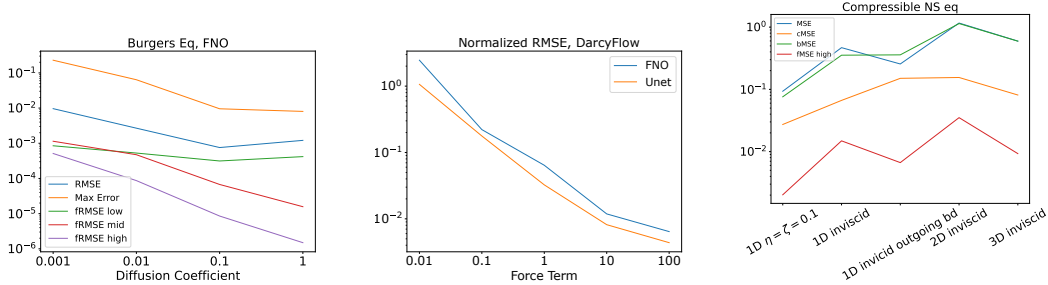


Figure 3: Detailed visualization of (a) Burgers’, (b) DarcyFlow, and (c) Compressible NS eqs.

4.2 Baseline Performance

Figure 2⁵ visualizes the RMSE performance of the surrogate models, averaged for each trained model over different PDE parameters. A more detailed comparison is shown in Appendix E.⁶ Among the baseline surrogate models, FNO provides the best prediction for most metrics. It learns the differential operators well, leading to low errors even for the conserved quantities and on the boundaries. Additionally, FNO has a consistent error of about 4×10^{-4} across the frequency spectrum for many problems highlighting its ability to learn in Fourier space. As an example, Figure 4 depicts the FNO and U-Net predictions for the 2D diffusion-reaction equation and the training data obtained from a numerical simulator. Our baseline results further indicate that the PINNs might deal better than expected with high-frequency features, despite prior observations [62]. As an example for an inverse problem setup, we identify the initial condition to minimize the prediction error of the ML surrogate over a 15 time steps horizon. In Figure 2b, we present the MSE of the prediction of estimated initial condition (with error bars) for 4 of the 11 datasets (1D). The results show that FNO outperforms U-Net also for the inverse problem. However, our benchmark also reveals several tasks which these methods cannot treat properly. First, Figure 3a shows that the FNO’s error increases with decreasing diffusion coefficient where a strong discontinuity appears. This can be attributed to Gibb’s phenomenon for FNO’s limited maximum wave frequency in Fourier space, as shown by an increase of two orders of magnitude for high-frequency fRMSE. Second, Figure 3b shows that the normalized RMSE increases with decreasing force term, which is equivalent to decreasing the scale-value of the solution (in our case, force term 0.01 means $\text{mean}(|u|) \approx 0.01$).⁷ Third, Figure 3c shows several metrics for the compressible Navier-Stokes equations. It shows the overall RMSE is very bad in comparison to the basic PDEs, such as the Burgers equation. Interestingly, the 3D inviscid case shows lower error than 2D inviscid case. We posit this is due to lower resolution resulting in smooth train/validation samples which FNO can learn very efficiently. This also indicates that high-resolution training samples should be used to create a surrogate model for real-world problems with a Reynolds number of more than 10^6 .

4.3 Temporal Error Analysis

Autoregressive Behaviour of U-Net We observed instabilities when training U-Net with fully autoregressive mode. When trained in an open loop, i.e. only 1 time step ahead without feedback of prediction, the error during testing quickly accumulates with more unrolled time steps. Therefore, we tried three different training methods as described in the previous section. Figure 5a shows the RMSE behaviour calculated at different unrolled time steps. It shows that for different U-Net training strategies, the RMSE behaviors are different. We observed that U-Net with the pushforward trick provides better stability during training for all problems, and better accuracy for a longer prediction horizon. For this reason, we used the U-Net with pushforward trick as our baseline score for U-Net.

⁵ In Figure 2 CFD means compressible fluid dynamics or, equivalently, the compressible Navier-Stokes equations.

⁶ Note that we omitted the PINN baseline score for the 2D/3D Compressible Navier-Stokes equations and the DarcyFlow. The reason for the former case is limited GPU memory, and the reason for the latter is that the DarcyFlow’s problem setup is to learn the mapping from diffusion coefficients $a(x)$ to a steady state solution, which cannot be treated by PINNs. ⁷ Note that U-Net is consistently better than FNO in this case. We postulate that this is due to the strong similarity between this task and the diffusion-like regression task that the original U-Net targets.

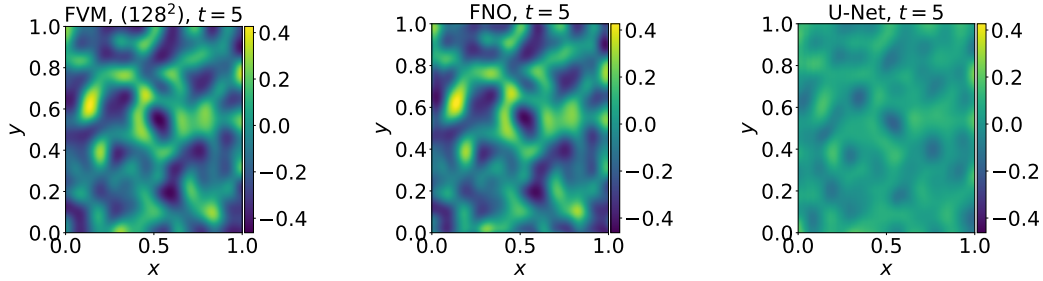


Figure 4: (a) Visualization of the 2D diffusion-reaction data generated with a standard finite volume (FVM) solver and a resolution of 128^2 , (b) FNO prediction, and (c) U-Net prediction.

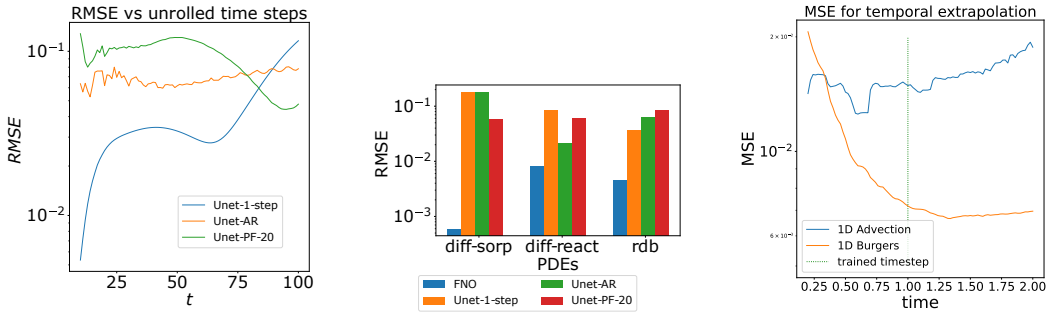


Figure 5: (a) Plots of the RMSE calculated at different unrolled time steps, (b) comparison of each autoregressive method, and (c) RMSE for temporal extrapolation.

Temporal Extrapolation Figure 5c plots the RMSE temporal evolution of 1D Advection and Burgers equations predicted using the FNO model. Different from the other scenarios, we trained only until half of the time steps used in the other cases (the green dotted line in the figure). The main purpose of this experiment is to test how well the ML model (FNO) learns the temporal dependency of the PDEs with limited information. We observe monotonically increasing errors after the time steps used in training ($t > 1$). This indicates that the present ML models cannot properly capture the dynamic behavior of the PDEs, and it is a challenging task to provide reliable predictions beyond the time experienced during training.

4.4 Inference Time Comparison

In this subsection, we provide runtime comparisons between the numerical PDE solvers that we use to generate a single data sample and the FNO, the most accurate ML model according to our experiments. A fair runtime comparison between classical solvers and ML methods is challenging because these method classes are usually optimized for different hardware setups. In this paper, we provide the information on the hardware and system configuration in Appendix F⁸. In addition, we list the ML models' total training time. All the runtime numbers are given in seconds. The highest computational demand originates from the ML training time. However, once the ML models were trained, the ML models' predictions can be computed multiple orders of magnitudes more efficiently. A more complete overview of these experiments can be found in Appendix F. The ML model allows us to predict a solution even in the strong-viscous regime ($\eta = \zeta = 0.1$) efficiently since it eliminates the stability restriction defined by the Courant-Friedrichs-Lewy condition [31]⁹. A more detailed analysis of the resolution sensitivity of inference time is provided in Appendix G.

⁸ We used the same hardware resources and system configuration for the 2D/3D CFD simulations and the ML methods. Whether or not this constitutes a fair comparison is surely debatable. ⁹ Note that in the table the ML inference and training time does not monotonically increase with spatial-dimension. This is because the 2D/3D cases' time-step numbers and training sample numbers is much smaller than Diffusion-sorption case.

| PDE | Resolution | Simulation time | ML inference time | ML training time |
|---------------------------------|--------------------|-----------------|-------------------|------------------|
| Diffusion-sorption | 1 024 ¹ | 59.83 | 0.32 | 48 760 |
| 2D CFD ($\eta = \zeta = 0.1$) | 512 ² | 582.61 | 0.14 | 107 567 |
| 3D CFD (inviscid) | 64 ³ | 60.06 | 0.14 | 12 387 |

5 Conclusions and Limitations

With PDEBENCH we contribute an extensive benchmark suite for comparing and evaluating methods on the realm of Scientific ML. We provide both pre-computed datasets for easy access in a dataverse as well as code to generate new data from configurable simulation runs. The focus is on time-dependent PDE problems ranging from simple 1D equations to challenging 3D coupled systems of equations featuring challenging boundary conditions. Furthermore, we present a variety of different evaluation metrics in order to better understand strengths and weaknesses of the machine learning methods in a scientific computing context. We also provide an example application for utilizing Scientific ML methods for inverse modeling with our benchmark data. We believe this will be an important area in the future for machine learning models to produce competitive results both in accuracy as well as runtime when compared to numerical methods.

Limitations While PDEBENCH provides an easy-to-use, modular and extensible approach to devising and testing ML surrogates for PDE simulations, the scope of our benchmark is naturally limited. Our main focus is on time-dependent PDEs for different types of flow problems which pose a wide variety of challenges to Scientific ML. We currently do not cover other types of physics nor quantum mechanics as this goes beyond the scope of this paper. With respect to flow problems, our main limitations are that we do not yet cover multi-phase flows or non-rectangular domains. This is left for future work.

Acknowledgements

We thank MinMae (John) Kim, Ran Zhang, Tianqi Wang, Yizhou Yang, Gefei Shan and Simon Brown of the ANU Techlauncher for consulting on code design and implementation. Partially funded by Deutsche Forschungsgemeinschaft (DFG, German Research Foundation) under Germany's Excellence Strategy - EXC 2075 – 390740016. We acknowledge support by the Stuttgart Center for Simulation Science (SimTech). We further thank the DaRUS-team, in particular Jan Range.

Checklist

1. For all authors...
 - (a) Do the main claims made in the abstract and introduction accurately reflect the paper's contributions and scope? **[Yes]** All the contributions listed in the abstract are elaborated in section 3.
 - (b) Did you describe the limitations of your work? **[Yes]** See the last paragraph of section 5.
 - (c) Did you discuss any potential negative societal impacts of your work? **[N/A]** We believe that our work does not have any potential negative societal impacts as it does not contain confidential or private data.
 - (d) Have you read the ethics review guidelines and ensured that your paper conforms to them? **[Yes]** We do not include any confidential or private data, only numerical values related to general physical systems with no potential ethical issues or severe environmental damage.
2. If you are including theoretical results...
 - (a) Did you state the full set of assumptions of all theoretical results? **[N/A]** We do not include any theoretical results.
 - (b) Did you include complete proofs of all theoretical results? **[N/A]** See the previous point.
3. If you ran experiments (e.g. for benchmarks)...
 - (a) Did you include the code, data, and instructions needed to reproduce the main experimental results (either in the supplemental material or as a URL)? **[Yes]** We include the parameters used to reproduce the datasets in Appendix D and instructions to run the code in the README file in our code repository.
 - (b) Did you specify all the training details (e.g., data splits, hyperparameters, how they were chosen)? **[Yes]** See Appendix C.
 - (c) Did you report error bars (e.g., with respect to the random seed after running experiments multiple times)? **[Yes]** We ran several experiments using different parameters. The mean and standard deviation values for the errors are reported in the Figure 2.
 - (d) Did you include the total amount of compute and the type of resources used (e.g., type of GPUs, internal cluster, or cloud provider)? **[Yes]** The types of GPUs used are provided in subsection 4.1.
4. If you are using existing assets (e.g., code, data, models) or curating/releasing new assets...
 - (a) If your work uses existing assets, did you cite the creators? **[Yes]** We adopted the implementation of the baseline models with some modifications, with proper citation and credits to the authors, as well as existing software packages.
 - (b) Did you mention the license of the assets? **[Yes]** Appropriate license notices are included in the affected source code files, and license of new assets is included in the supplementary materials.
 - (c) Did you include any new assets either in the supplemental material or as a URL? **[Yes]** All the data generation scripts are included in the code repository.
 - (d) Did you discuss whether and how consent was obtained from people whose data you're using/curating? **[N/A]** We generate all of our data, and the models we use are all openly accessible to the public, so we adopt and modify them, and include citations to the original authors.

- (e) Did you discuss whether the data you are using/curating contains personally identifiable information or offensive content? [N/A] We do not include any personal information or offensive content in our datasets.
5. If you used crowdsourcing or conducted research with human subjects...
- (a) Did you include the full text of instructions given to participants and screenshots, if applicable? [N/A] We use neither crowdsourcing nor conduct research with human subjects.
- (b) Did you describe any potential participant risks, with links to Institutional Review Board (IRB) approvals, if applicable? [N/A] See the previous point.
- (c) Did you include the estimated hourly wage paid to participants and the total amount spent on participant compensation? [N/A] See the previous point.

References

- [1] K. R. Allen, T. Lopez-Guevara, K. Stachenfeld, A. Sanchez-Gonzalez, P. Battaglia, J. Hamrick, and T. Pfaff. Physical design using differentiable learned simulators. *arXiv preprint arXiv:2202.00728*, 2022.
- [2] F. d. A. Belbute-Peres, Y.-f. Chen, and F. Sha. Hyperpinn: Learning parameterized differential equations with physics-informed hypernetworks. In *International Conference on Learning Representations*, 2021. URL <https://openreview.net/pdf?id=LxUuRDUhRjM>.
- [3] D. A. Bezgin, A. B. Buhendwa, and N. A. Adams. JAX-FLUIDS: A fully-differentiable high-order computational fluid dynamics solver for compressible two-phase flows, 2022. URL <https://arxiv.org/abs/2203.13760>.
- [4] J. Brandstetter, D. Worrall, and M. Welling. Message passing neural pde solvers. In *The Tenth International Conference on Learning Representations*, 2022. URL <https://openreview.net/pdf?id=vSix3HPYKSU>.
- [5] G. Brockman, V. Cheung, L. Pettersson, J. Schneider, J. Schulman, J. Tang, and W. Zaremba. OpenAI Gym, 2016.
- [6] S. L. Brunton and J. N. Kutz. *Data-Driven Science and Engineering: Machine Learning, Dynamical Systems, and Control*. Cambridge University Press, 2019. ISBN 978-1-108-42209-3. URL <https://databookuw.com>.
- [7] K. Cao. *Inverse Problems for the Heat Equation Using Conjugate Gradient Methods*. PhD thesis, University of Leeds, 2018.
- [8] T. Q. Chen, Y. Rubanova, J. Bettencourt, and D. K. Duvenaud. Neural ordinary differential equations. In S. Bengio, H. Wallach, H. Larochelle, K. Grauman, N. Cesa-Bianchi, and R. Garnett, editors, *Advances in Neural Information Processing Systems 31*, pages 6572–6583. Curran Associates, Inc., 2018.
- [9] M. Chu, N. Thuerey, H.-P. Seidel, C. Theobalt, and R. Zayer. Learning meaningful controls for fluids. *ACM Transactions on Graphics*, 40(4):1–13, Aug. 2021. doi: 10.1145/3476576.3476661.
- [10] M. Crosas. The dataverse network: An open-source application for sharing, discovering and preserving data. *D-Lib Magazine*, Volume 17, 2011. URL <http://www.dlib.org/dlib/january11/crosas/01crosas.html>.
- [11] H. Eivazi, M. Tahani, P. Schlatter, and R. Vinuesa. Physics-informed neural networks for solving reynolds-averaged navier-stokes equations. *arXiv:2107.10711 [physics]*, Jul 2021. URL <http://arxiv.org/abs/2107.10711>. arXiv: 2107.10711.
- [12] R. P. Feynman. *Feynman lectures on physics - Volume 1*. 1963.
- [13] C. D. Freeman, E. Frey, A. Raichuk, S. Girgin, I. Mordatch, and O. Bachem. Brax—a differentiable physics engine for large scale rigid body simulation. *arXiv preprint arXiv:2106.13281*, 2021. URL <https://datasets-benchmarks-proceedings.neurips.cc/paper/2021/file/3def184ad8f4755ff269862ea77393dd-Paper-round1.pdf>.

- [14] D. W. Gladish, D. E. Pagendam, L. J. M. Peeters, P. M. Kuhnert, and J. Vaze. Emulation Engines: Choice and Quantification of Uncertainty for Complex Hydrological Models. *Journal of Agricultural, Biological and Environmental Statistics*, 23(1):39–62, Mar. 2018. doi: 10.1007/s13253-017-0308-3.
- [15] T. H. Group. An overview of the hdf5 technology suite and its applications, 2022. URL <https://portal.hdfgroup.org/display/HDF5/HDF5>.
- [16] M. Guo and J. S. Hesthaven. Data-driven reduced order modeling for time-dependent problems. *Computer Methods in Applied Mechanics and Engineering*, 345:75–99, 2019. ISSN 0045-7825. doi: <https://doi.org/10.1016/j.cma.2018.10.029>. URL <https://www.sciencedirect.com/science/article/pii/S0045782518305334>.
- [17] O. Hennigh, S. Narasimhan, M. A. Nabian, A. Subramaniam, K. Tangsali, M. Rietmann, J. d. A. Ferrandis, W. Byeon, Z. Fang, and S. Choudhry. NVIDIA SimNetTM: An AI-accelerated multi-physics simulation framework. *arXiv:2012.07938 [physics]*, Dec. 2020.
- [18] P. Holl and V. Koltun. Phiflow: A differentiable PDE solving framework for deep learning via physical simulations. page 5, 2020.
- [19] Z. Huang, T. Schneider, M. Li, C. Jiang, D. Zorin, and D. Panozzo. A large-scale benchmark for the incompressible Navier-Stokes equations, 2021. URL <https://arxiv.org/abs/2112.05309>.
- [20] T. Inoue, S.-i. Inutsuka, and H. Koyama. The Role of Ambipolar Diffusion in the Formation Process of Moderately Magnetized Diffuse Clouds. *The Astrophysical Journal*, 658(2):L99–L102, Apr. 2007. doi: 10.1086/514816.
- [21] M. Karlbauer, T. Praditia, S. Otte, S. Oladyshkin, W. Nowak, and M. V. Butz. Composing partial differential equations with physics-aware neural networks. In *Proceedings of the 39th International Conference on Machine Learning*, Proceedings of Machine Learning Research, Baltimore, USA, 16–23 Jul 2022.
- [22] K. Kashinath, M. Mustafa, A. Albert, J.-L. Wu, C. Jiang, S. Esmaeilzadeh, K. Azizzadenesheli, R. Wang, A. Chattopadhyay, A. Singh, A. Manepalli, D. Chirila, R. Yu, R. Walters, B. White, H. Xiao, H. A. Tchelepi, P. Marcus, A. Anandkumar, P. Hassanzadeh, and n. Prabhat. Physics-informed machine learning: Case studies for weather and climate modelling. *Philosophical Transactions of the Royal Society A: Mathematical, Physical and Engineering Sciences*, 379(2194):20200093, Apr. 2021. doi: 10.1098/rsta.2020.0093.
- [23] D. I. Ketcheson, K. T. Mandli, A. J. Ahmadi, A. Alghamdi, M. Quezada de Luna, M. Parsani, M. G. Knepley, and M. Emmett. PyClaw: Accessible, Extensible, Scalable Tools for Wave Propagation Problems. *SIAM Journal on Scientific Computing*, 34(4):C210–C231, Nov. 2012.
- [24] D. P. Kingma and J. Ba. Adam: A method for stochastic optimization. *arXiv preprint arXiv:1412.6980*, 2014.
- [25] G. Klaasen and W. Troy. Stationary wave solutions of a system of reaction-diffusion equations derived from the fitzhugh–nagumo equations. *SIAM Journal on Applied Mathematics*, 44(1): 96–110, 1984. doi: 10.1137/0144008.
- [26] N. Kovachki, Z. Li, B. Liu, K. Azizzadenesheli, K. Bhattacharya, A. Stuart, and A. Anandkumar. Neural operator: Learning Maps Between Function Spaces. *arXiv:2108.08481 [cs, math]*, Sept. 2021.
- [27] A. Krishnapriyan, A. Gholami, S. Zhe, R. Kirby, and M. W. Mahoney. Characterizing possible failure modes in physics-informed neural networks. *Advances in Neural Information Processing Systems*, 34, 2021.
- [28] A. Lavin, H. Zenil, B. Paige, D. Krakauer, J. Gottschlich, T. Mattson, A. Anandkumar, S. Choudry, K. Rocki, A. G. Baydin, C. Prunkl, B. Paige, O. Isayev, E. Peterson, P. L. McMahon, J. Macke, K. Cranmer, J. Zhang, H. Wainwright, A. Hanuka, M. Veloso, S. Assefa, S. Zheng, and A. Pfeffer. Simulation Intelligence: Towards a New Generation of Scientific Methods. *arXiv:2112.03235 [cs]*, Dec. 2021.

- [29] R. Leiteritz, M. Hurler, and D. Pflüger. Learning free-surface flow with physics-informed neural networks. In *2021 20th IEEE International Conference on Machine Learning and Applications (ICMLA)*, pages 1668–1673, 2021. doi: 10.1109/ICMLA52953.2021.00266.
- [30] R. Leiteritz, P. Buchfink, B. Haasdonk, and D. Pflüger. Surrogate-data-enriched physics-aware neural networks. *Proceedings of the Northern Lights Deep Learning Workshop*, 2, 04 2022. doi: 10.7557/18.6268.
- [31] H. Lewy, K. Friedrichs, and R. Courant. Über die partiellen differenzgleichungen der mathematischen physik. *Mathematische annalen*, 100:32–74, 1928.
- [32] Z. Li, N. Kovachki, K. Azizzadenesheli, B. Liu, K. Bhattacharya, A. Stuart, and A. Anandkumar. Fourier neural operator for parametric partial differential equations. *International Conference on Learning Representations (ICLR)*, 2021.
- [33] G. Limousin, J.-P. Gaudet, L. Charlet, S. Szenknect, V. Barthès, and M. Krimissa. Sorption isotherms: A review on physical bases, modeling and measurement. *Applied Geochemistry*, 22(2):249–275, 2007. ISSN 0883-2927. doi: <https://doi.org/10.1016/j.apgeochem.2006.09.010>. URL <https://www.sciencedirect.com/science/article/pii/S0883292706002629>.
- [34] L. Lu, X. Meng, Z. Mao, and G. E. Karniadakis. DeepXDE: A deep learning library for solving differential equations. *SIAM Review*, 63(1):208–228, 2021. doi: 10.1137/19M1274067.
- [35] D. MacKinlay, D. Pagendam, P. M. Kuhnert, T. Cui, D. Robertson, and S. Janardhanan. Model Inversion for Spatio-temporal Processes using the Fourier Neural Operator. In *Neurips Workshop on Machine Learning for the Physical Sciences*, page 7, 2021.
- [36] S. Makridakis, E. Spiliotis, and V. Assimakopoulos. The M4 Competition: 100,000 time series and 61 forecasting methods. *International Journal of Forecasting*, 36(1):54–74, Jan. 2020. doi: 10.1016/j.ijforecast.2019.04.014.
- [37] S. K. Mitusch, S. W. Funke, and J. S. Dokken. Dofin-Adjoint 2018.1: Automated adjoints for FEniCS and Firedrake. *Journal of Open Source Software*, 4(38):1292, June 2019. doi: 10.21105/joss.01292.
- [38] J. Močkus. On Bayesian Methods for Seeking the Extremum. In G. I. Marchuk, editor, *Optimization Techniques IFIP Technical Conference: Novosibirsk, July 1–7, 1974*, Lecture Notes in Computer Science, pages 400–404, Berlin, Heidelberg, 1975. Springer. ISBN 978-3-662-38527-2. doi: 10.1007/978-3-662-38527-2_55.
- [39] F. Moukalled, L. Mangani, and M. Darwish. *The Finite Volume Method in Computational Fluid Dynamics*. Springer, 1 edition, 2016. doi: 10.1007/978-3-319-16874-6.
- [40] J. Nocedal and S. J. Wright. *Numerical optimization*. Springer, 1999.
- [41] W. Nowak and A. Guthke. Entropy-based experimental design for optimal model discrimination in the geosciences. *Entropy*, 18(11), 2016. doi: 10.3390/e18110409.
- [42] A. O’Hagan. Curve Fitting and Optimal Design for Prediction. *Journal of the Royal Statistical Society: Series B (Methodological)*, 40(1):1–24, 1978. doi: 10.1111/j.2517-6161.1978.tb01643.x.
- [43] R. S. Olson, W. La Cava, P. Orzechowski, R. J. Urbanowicz, and J. H. Moore. PMLB: A large benchmark suite for machine learning evaluation and comparison. *BioData Mining*, 10(1):36, Dec. 2017. doi: 10.1186/s13040-017-0154-4.
- [44] K. Otness, A. Gjoka, J. Bruna, D. Panozzo, B. Peherstorfer, T. Schneider, and D. Zorin. An extensible benchmark suite for learning to simulate physical systems. In *Thirty-fifth Conference on Neural Information Processing Systems Datasets and Benchmarks Track (Round 1)*, 2021. URL <https://openreview.net/forum?id=pY9MHwmrymR>.

- [45] A. Paszke, S. Gross, F. Massa, A. Lerer, J. Bradbury, G. Chanan, T. Killeen, Z. Lin, N. Gimelshein, L. Antiga, A. Desmaison, A. Kopf, E. Yang, Z. DeVito, M. Raison, A. Tejani, S. Chilamkurthy, B. Steiner, L. Fang, J. Bai, and S. Chintala. Pytorch: An imperative style, high-performance deep learning library. In H. Wallach, H. Larochelle, A. Beygelzimer, F. d'Alché-Buc, E. Fox, and R. Garnett, editors, *Advances in Neural Information Processing Systems 32*, pages 8024–8035. Curran Associates, Inc., 2019. URL <http://papers.neurips.cc/paper/9015-pytorch-an-imperative-style-high-performance-deep-learning-library.pdf>.
- [46] C. Rackauckas. The essential tools of scientific machine learning (Scientific ML). *The Winnower*, Aug. 2019. doi: 10.15200/winn.156631.13064.
- [47] M. Raissi, P. Perdikaris, and G. E. Karniadakis. Physics-informed neural networks: A deep learning framework for solving forward and inverse problems involving nonlinear partial differential equations. *Journal of Computational Physics*, 378:686–707, Feb. 2019. doi: 10.1016/j.jcp.2018.10.045.
- [48] O. Ronneberger, P. Fischer, and T. Brox. U-Net: Convolutional Networks for Biomedical Image Segmentation, May 2015.
- [49] L. Ruthotto and E. Haber. Deep Neural Networks motivated by Partial Differential Equations. *arXiv:1804.04272 [cs, math, stat]*, Apr. 2018.
- [50] J. Snoek, H. Larochelle, and R. P. Adams. Practical bayesian optimization of machine learning algorithms. In *Advances in Neural Information Processing Systems*, pages 2951–2959. Curran Associates, Inc., 2012.
- [51] K. Stachenfeld, D. B. Fielding, D. Kochkov, M. Cranmer, T. Pfaff, J. Godwin, C. Cui, S. Ho, P. Battaglia, and A. Sanchez-Gonzalez. Learned coarse models for efficient turbulence simulation, 2022. URL <https://arxiv.org/abs/2112.15275>.
- [52] J. M. Stone and M. L. Norman. ZEUS-2D: A Radiation Magnetohydrodynamics Code for Astrophysical Flows in Two Space Dimensions. I. The Hydrodynamic Algorithms and Tests. *The Astrophysical Journal Supplement*, 80:753, June 1992. doi: 10.1086/191680.
- [53] A. M. Stuart. Inverse problems: A Bayesian perspective. *Acta Numerica*, 19:451–559, 2010. doi: 10.1017/S0962492910000061.
- [54] D. J. Tait and T. Damoulas. Variational Autoencoding of PDE Inverse Problems. *arXiv:2006.15641 [cs, stat]*, June 2020.
- [55] M. Takamoto, T. Pradita, R. Leiteritz, D. MacKinlay, F. Alesiani, D. Pflüger, and M. Niepert. PDEBench: A diverse and comprehensive benchmark for scientific machine learning, 2022. URL <https://darus.uni-stuttgart.de/privateurl.xhtml?token=1be27526-348a-40ed-9fd0-c62f588efc01>.
- [56] A. Tarantola. *Inverse Problem Theory and Methods for Model Parameter Estimation*. SIAM, Jan. 2005. ISBN 978-0-89871-792-1.
- [57] E. F. Toro, M. Spruce, and W. Speares. Restoration of the contact surface in the HLL-Riemann solver. *Shock Waves*, 4(1):25–34, July 1994. doi: 10.1007/BF01414629.
- [58] A. Turing. The chemical basis of morphogenesis. *Philosophical Transactions of the Royal Society B*, 237:37–72, 1952.
- [59] B. van Leer. Towards the Ultimate Conservative Difference Scheme. V. A Second-Order Sequel to Godunov’s Method. *Journal of Computational Physics*, 32(1):101–136, July 1979. doi: 10.1016/0021-9991(79)90145-1.
- [60] P. Virtanen, R. Gommers, T. E. Oliphant, M. Haberland, T. Reddy, D. Cournapeau, E. Burovski, P. Peterson, W. Weckesser, J. Bright, S. J. van der Walt, M. Brett, J. Wilson, K. J. Millman, N. Mayorov, A. R. J. Nelson, E. Jones, R. Kern, E. Larson, C. J. Carey, Í. Polat, Y. Feng, E. W. Moore, J. VanderPlas, D. Laxalde, J. Perktold, R. Cimrman, I. Henriksen, E. A. Quintero,

- C. R. Harris, A. M. Archibald, A. H. Ribeiro, F. Pedregosa, P. van Mulbregt, and SciPy 1.0 Contributors. SciPy 1.0: Fundamental Algorithms for Scientific Computing in Python. *Nature Methods*, 17:261–272, 2020. doi: 10.1038/s41592-019-0686-2.
- [61] R. Wang, K. Kashinath, M. Mustafa, A. Albert, and R. Yu. Towards Physics-informed Deep Learning for Turbulent Flow Prediction. *arXiv:1911.08655 [physics, stat]*, June 2020.
- [62] S. Wang, X. Yu, and P. Perdikaris. When and why pinns fail to train: A neural tangent kernel perspective. *Journal of Computational Physics*, 449:110768, 2022. ISSN 0021-9991. doi: <https://doi.org/10.1016/j.jcp.2021.110768>. URL <https://www.sciencedirect.com/science/article/pii/S002199912100663X>.
- [63] M. D. Wilkinson, M. Dumontier, I. J. Aalbersberg, G. Appleton, M. Axton, A. Baak, N. Blomberg, J.-W. Boiten, L. B. da Silva Santos, P. E. Bourne, et al. The fair guiding principles for scientific data management and stewardship. *Scientific data*, 3(1):1–9, 2016.
- [64] O. Yadan. Hydra - a framework for elegantly configuring complex applications. Github, 2019. URL <https://github.com/facebookresearch/hydra>.

PDEBENCH: An Extensive Benchmark for Scientific Machine Learning. Supplementary Material ¹⁰

A Continuation of Related Work

Benchmarks in machine learning are an ubiquitous feature of the field. In recent years, their design and implementation has become a research area of its own right. Easily accessible and widely used image classification benchmarks such as MNIST and ImageNet are widely credited with accelerating progress in machine learning. Various domains in machine learning have widely influential datasets: In time series forecasting there are the Makridakis competitions [36], in reinforcement learning there is the OpenAI Gym [5]. Generic classification problems use, for example, the Penn Machine Learning Benchmark [43].

Closely related to the chosen Scientific ML baselines is the problem of directly differentiating through the numerical solver, which can itself be used in training an approximating model, or to directly solve some optimization or control problem of interest. Differentiable direct PDE solvers are increasingly available, e.g. [37] and frequently built upon neural network technology stacks [13, 3, 18].

Recent efforts have attempted to unify Scientific ML surrogates for PDEs under a single interface. For example, NVIDIA’s MODULUS/SimNet [17] implements a variety of methods in a single framework, although unfortunately under onerous intellectual property restrictions and an opaque contribution process. The DeepXDE project [34] is available under an open license and provides an impressive range of capabilities, but is largely restricted to PINN and DeepONet methods [47].

B Detailed metrics description

The classic loss metrics we use are (1) root-mean-squared-error (RMSE), (2) normalized RMSE (nRMSE), (3) maximum error. These measure the emulating model’s global performance but neglect local performance. Thus we include extra metrics to measure specific failure modes: (4) RMSE of the conserved value (cRMSE), (5) RMSE at boundaries (bRMSE), (6) RMSE in Fourier space (fRMSE) constrained to low, middle, and high-frequency regions.

The normalized RMSE is a variant of the RMSE to provide scale-independent information defined as:

$$\text{nRMSE} \equiv \frac{\|u_{\text{pred}} - u_{\text{true}}\|_2}{\|u_{\text{true}}\|_2}, \quad (4)$$

where $\|u\|_2$ is the L_2 -norm of a (vector-valued) variable u , and $u_{\text{true}}, u_{\text{pred}}$ are true and predicted value, respectively. The maximum error measures the model’s worst prediction, which quantifies both local performance and models’ stability of their prediction. cRMSE is defined as $\text{nRMSE} \equiv \|\sum u_{\text{pred}} - \sum u_{\text{true}}\|_2/N$, which measure the deviation of the prediction from some physically conserved value. bRMSE measures the error at the boundary, indicating if the model understand the boundary condition properly. Finally, fRMSE measures the error in low/middle/high-frequency ranges defined as

$$\sqrt{\frac{\sum_{k_{\min}}^{k_{\max}} |\mathcal{F}(u_{\text{pred}}) - \mathcal{F}(u_{\text{true}})|^2}{k_{\max} - k_{\min} + 1}}, \quad (5)$$

where \mathcal{F} is a discrete Fourier transformation, and k_{\min}, k_{\max} are the minimum and maximum indices in Fourier coordinates. In our paper, we define the low/middle/high-frequency regions as Low: $k_{\min} = 0, k_{\max} = 4$, Middle: $k_{\min} = 5, k_{\max} = 12$, and High: $k_{\min} = 13, k_{\max} = \infty$. This allows a quantitative discussion of the model performance’s dependence on the wavelength. In the multi-dimensional cases, we first integrate the angular coordinate direction of $|\mathcal{F}[u_{\text{pred}} - u_{\text{true}}](k)|^2$, and take the sum along the k -coordinate.

B.1 Inverse Problem Metrics

For the inverse problem setup, we selected various metrics. The major difference with respect to the forward metrics is that we have two main quantities to measure:

¹⁰ PDEBENCH repository <https://github.com/pdebench/PDEBench>.

- the error of the *quantity* we want to estimate, in our case the initial condition u_0 :

$$\mathcal{L}(u_0, \hat{u}_0)$$

where \hat{u}_0 is the estimated value;

- the error of the *prediction* based on the estimated initial condition $u(t, x|u_0)$,

$$\mathcal{L}(u(t, x|u_0), u(t, x|\hat{u}_0))$$

In general, we expect a larger error when we measure the error in the estimated quantity w.r.t. the predicted quantity. This is mainly due to the early decay of high frequencies of the PDE. We evaluated the error of the prediction at a specific instant in time $t = T$, that has been selected as $T = 15$ for all the tested datasets, expect $T = 5$ for the CFD dataset.

The metrics that we used for the inverse problem are: 1) MSE 2) the normalized ℓ_2 norm (L2), 3) the normalized ℓ_3 norm (L3); 4) the FFT MSE, the FFT L2 and 5) the FFT L3. For the frequency metrics we investigated the low frequency (between 0 and 1/4 of the max frequency), the middle frequency (between 1/4 and 3/4) and high frequency (between 3/4 and the maximum frequency) ranges. In Fig.12, the right figure shows the frequency power density, where we see that the largest error is found in the middle frequency range.

C Training Protocol and Hyperparameters

The model was trained for 500 epochs with the Adam optimizer [24] as per the protocol of the original FNO. The initial learning rate was set as 10^{-3} and reduced by half after each 100 epochs. The datasets are split into 90% training and 10% validation and testing. For the PINNs, we use DeepXDE [34] implementation. The training was performed for 15,000 epochs with the Adam optimizer, with the learning rate set to 10^{-3} . As with the example problems from that library we use a fully-connected network of depth 6 with 40 neurons each. In contrast to the other surrogate models, the PINN baseline can be trained and tested only on a single sample, and is valid only for a specific initial and boundary condition. To get more reliable error bounds, we thus chose to train the PINN baseline for 10 different samples per dataset and average the resulting error metrics.

C.1 Inverse problem

For testing the power of surrogate models to solve inverse problems, we consider a simplified scenario where the machine learning model directly predicts a specific time in the future $t = T$. When training to predict a specific time in the future, we reduce the training time and avoid to consider the effect of training approaches (as discussed in the temporal analysis section subsection 4.3) in evaluating the surrogate models. We trained over $N_{\text{epoch}} = 20$ epochs and we selected as final time step $T = 15$ for all tested datasets, expect for the CFD dataset where we selected $T = 5$. We used similar parameters used in the forward training, while we selected 64 hidden values to be estimated for the initial condition and 100 samples to test and 0.2 as learning rate for the gradient method. The loss function for the gradient computation is the MSE.

D Detailed Problem Description

In this section, we provide more detailed descriptions of each PDE and its applications. Note that PDE is the basic mathematical tool to describe the evolution of the system in physics. Interested readers are referred to representative textbooks of physics, for example, [12].

D.1 1D Advection Equation

The advection equation models pure advection behavior without non-linearity whose expression is given as:

$$\partial_t u(t, x) + \beta \partial_x u(t, x) = 0, \quad x \in (0, 1), t \in (0, 2], \quad (6)$$

$$u(0, x) = u_0(x), \quad x \in (0, 1), \quad (7)$$

where β is a constant advection speed. Note that the exact solution of the system is given as: $u(t, x) = u_0(x - \beta t)$.

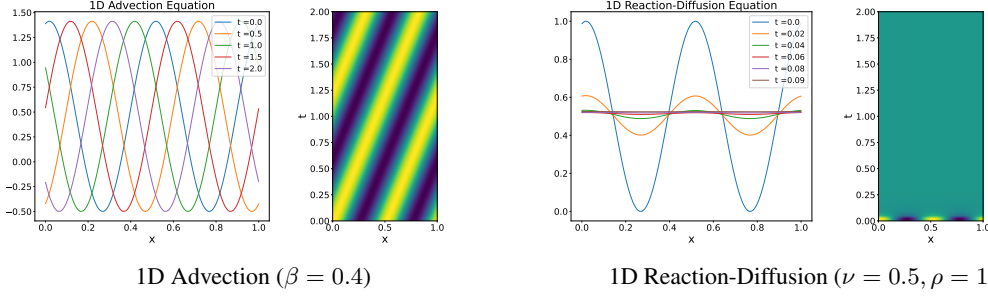


Figure 6: Visualization of the time evolution of 1D Advection equation and Reaction-Diffusion equation.

In our dataset, we only considered the periodic boundary condition. As an initial condition, we use a super-position of sinusoidal waves as:

$$u_0(x) = \sum_{k_i=k_1, \dots, k_N} A_i \sin(k_i x + \phi_i), \quad (8)$$

where $k_i = 2\pi\{n_i\}/L_x$ are wave numbers whose $\{n_i\}$ are integer numbers selected randomly in $[1, n_{\max}]$, N is the integer determining how many waves to be added, L_x is the calculation domain size, A_i is a random float number uniformly chosen in $[0, 1]$, and ϕ_i is the randomly chosen phase in $(0, 2\pi)$. In 1D-advection case, we set $k_{\max} = 8$ and $N = 2$. After calculating Equation 8, we randomly operate the absolute value function with random signature and the window-function with 10% probability, respectively.

The numerical solution was calculated with the temporally and spatially 2nd-order upwind finite difference scheme.

D.2 1D Diffusion-Reaction Equation

Here, we consider a one-dimensional diffusion-reaction type PDE, that combines a diffusion process and a rapid evolution from a source term [27]. The equation is expressed as:

$$\partial_t u(t, x) - \nu \partial_{xx} u(t, x) - \rho u(1 - u) = 0, \quad x \in (0, 1), t \in (0, 1], \quad (9)$$

$$u(0, x) = u_0(x), \quad x \in (0, 1). \quad (10)$$

Note that the variable u develops at potentially exponential rate because of the force term which depends on u . measure the ability to capture very rapid dynamics.

Similar to the 1D advection equation case, we use the periodic boundary condition and Equation 8 as the initial condition. To avoid an ill-defined initial condition, we also applied the absolute value function and a normalization operation, dividing the initial condition by the maximum value. The numerical solution was calculated with the temporally and spatially 2nd-order central difference scheme. For the source term part, we use the piecewise-exact solution (PES) method [20].

D.3 Burgers equation

The Burgers' equation is a PDE modeling the non-linear behavior and diffusion process in fluid dynamics as

$$\partial_t u(t, x) + \partial_x(u^2(t, x)/2) = \nu/\pi \partial_{xx} u(t, x), \quad x \in (0, 1), t \in (0, 2], \quad (11)$$

$$u(0, x) = u_0(x), \quad x \in (0, 1), \quad (12)$$

where ν is the diffusion coefficient, which is assumed constant in our dataset.

Note that setting $R \equiv \pi u L / \nu$ describes the system's evolution as the Reynolds number of the Navier-Stokes equation (2); $R > 1$ means the strong non-linear case support forming shock phenomena, and $R < 1$ means the diffusive case.

Similar to the 1D advection equation case, we use the periodic boundary condition and Equation 8 as the initial condition. The numerical solution was calculated with the temporally and spatially

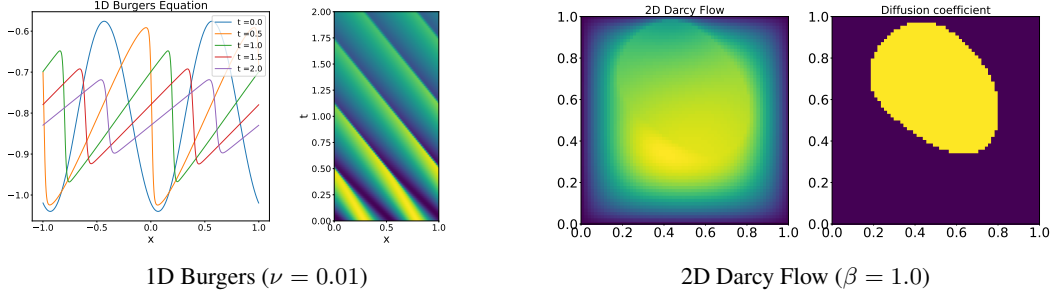


Figure 7: Visualization of the time evolution of 1D Burgers equation and 2D Darcy Flow.

2nd-order upwind difference scheme for the advection term, and the central difference scheme for the diffusion term.

D.4 Darcy Flow

We experiment with the steady-state solution of 2D Darcy Flow over the unit square, whose viscosity term $a(x)$ is an input of the system. The solution of the steady-state is defined by the following equation

$$-\nabla(a(x)\nabla u(x)) = f(x), \quad x \in (0,1)^2, \quad (13)$$

$$u(x) = 0, \quad x \in \partial(0,1)^2. \quad (14)$$

In this paper, the force term f is set as a constant value β , changing the scale of the solution $u(x)$. Instead of directly solving Equation 13, we obtained the solution by solving a temporal evolution equation:

$$\partial_t u(x,t) - \nabla(a(x)\nabla u(x,t)) = f(x), \quad x \in (0,1)^2, \quad (15)$$

with random field initial condition, until reaching a steady state. The numerical calculation was performed the same as the case of the 1D Diffusion-Reaction equation.

D.5 Compressible Navier-Stokes equation

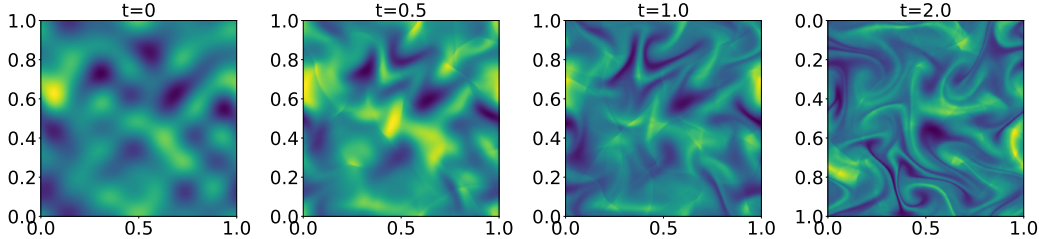


Figure 8: Visualization of the time evolution of the density in the case of 2D Compressible Navier-Stokes equations (inviscid, $M = 0.1$).

The compressible fluid dynamic equations describe a fluid flow,

$$\partial_t \rho + \nabla \cdot (\rho \mathbf{v}) = 0, \quad (16a)$$

$$\rho(\partial_t \mathbf{v} + \mathbf{v} \cdot \nabla \mathbf{v}) = -\nabla p + \eta \Delta \mathbf{v} + (\zeta + \eta/3) \nabla(\nabla \cdot \mathbf{v}), \quad (16b)$$

$$\partial_t \left[\epsilon + \frac{\rho v^2}{2} \right] + \nabla \cdot \left[\left(\epsilon + p + \frac{\rho v^2}{2} \right) \mathbf{v} - \mathbf{v} \cdot \sigma' \right] = 0, \quad (16c)$$

where ρ is the mass density, \mathbf{v} is the velocity, p is the gas pressure, $\epsilon = p/(\Gamma - 1)$ is the internal energy, $\Gamma = 5/3$, σ' is the viscous stress tensor, and η, ζ are the shear and bulk viscosity, respectively.

PDEBENCH provides the following training datasets for the compressible Navier-Stokes equations:

| N_d | initial field | boundary condition | (η, ζ, M) |
|-------|---------------|--------------------|---------------------------|
| 1D | random field | periodic | $(10^{-8}, 10^{-8}, -)$ |
| 1D | random field | periodic | $(10^{-2}, 10^{-2}, -)$ |
| 1D | random field | periodic | $(10^{-1}, 10^{-1}, -)$ |
| 1D | random field | out-going | $(10^{-8}, 10^{-8}, -)$ |
| 1D | shock-tube | out-going | $(10^{-8}, 10^{-8}, -)$ |
| 2D | random field | periodic | $(10^{-8}, 10^{-8}, 0.1)$ |
| 2D | random field | periodic | $(10^{-2}, 10^{-2}, 0.1)$ |
| 2D | random field | periodic | $(10^{-1}, 10^{-1}, 0.1)$ |
| 2D | random field | periodic | $(10^{-8}, 10^{-8}, 1.0)$ |
| 2D | random field | periodic | $(10^{-2}, 10^{-2}, 1.0)$ |
| 2D | random field | periodic | $(10^{-1}, 10^{-1}, 1.0)$ |
| 2D | turbulence | periodic | $(10^{-8}, 10^{-8}, 0.1)$ |
| 2D | turbulence | periodic | $(10^{-8}, 10^{-8}, 1.0)$ |
| 3D | random field | periodic | $(10^{-8}, 10^{-8}, 1.0)$ |
| 3D | random field | periodic | $(10^{-2}, 10^{-2}, 1.0)$ |

where N_d is the number of spatial dimensions, $M = |v|/c_s$ is the Mach number, $c_s = \sqrt{\Gamma p/\rho}$ is the sound velocity. The outgoing boundary condition is copying the neighbor cell to the boundary region which allows waves and fluid to escape from the computational domain, and is popular for astrohydrodynamics simulations [52]. The random field initial condition is applying Equation 8 which is extended to higher dimensions for the 2D and 3D cases. Note that density and pressure are prepared by adding a uniform background to the perturbation field Equation 8. The turbulence initial condition considers turbulent velocity with uniform mass density and pressure. The velocity is calculated similarly to Equation 8 as

$$\mathbf{v}(x, t = 0) = \sum_{i=1}^n \mathbf{A}_i \sin(k_i x + \phi_i), \quad (17)$$

where $n = 4$ and $A_i = \bar{v}/|k|^d$, and $d = 1, 2$ when considering 2D and 3D, respectively. \bar{v} is determined by the initial Mach number as $\bar{v} = c_s M$. To reduce the compressibility effect, we subtracted the compressible field from Equation 17 by the Helmholtz-decomposition in the Fourier space.

The shock-tube initial field is composed as $Q(x, t = 0) = (Q_L, Q_R)$, where $Q = (\rho, \mathbf{v}, p)$ and Q_L, Q_R are randomly determined constant values. The location of the initial discontinuity is also randomly determined. This problem is called the "Riemann problem", and the initial discontinuity generates shocks and rarefaction depending on the values of Q_L, Q_R , which are very difficult to obtain without solving the PDEs. This scenario can be used for a rigorous test if ML models fully understand Equation 16a - Equation 16c. The numerical solution was calculated with the temporally and spatially 2nd-order HLLC scheme [57] with the MUSCL method [59] for the inviscid part, and the central difference scheme for the viscous part.

D.6 Inhomogenous, incompressible Navier-Stokes

A popular simplification of the Navier-Stokes equation is the incompressible version, commonly used to model dynamics supposed to be far lower than the speed of propagation of waves in the medium,

$$\nabla \cdot \mathbf{v} = 0, \quad \rho(\partial_t \mathbf{v} + \mathbf{v} \cdot \nabla \mathbf{v}) = -\nabla p + \eta \Delta \mathbf{v}. \quad (18)$$

These simplify the compressible Navier-Stokes equations Eq. (2), by substituting the first term in Eq. (18) instead of the first term in (16), from which we can eliminate several elements in the second terms of Eq. (18). Additionally, we have introduced the assumption that the fluid is homogeneous (i.e. not a fluid comprising two or more substances of different density or viscosity).

We employ an augmented form of (18) which includes a vector field *forcing* term \mathbf{u} ,

$$\rho(\partial_t \mathbf{v} + \mathbf{v} \cdot \nabla \mathbf{v}) = -\nabla p + \eta \Delta \mathbf{v} + \mathbf{u}. \quad (19)$$

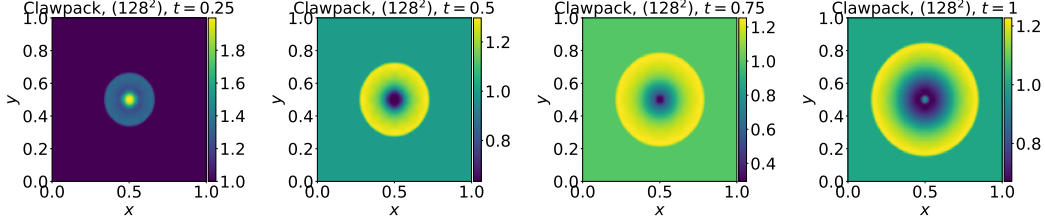


Figure 9: Visualization of the time evolution of the 2D shallow-water equations data.

Non-periodic conditions are included to challenge models which perform well upon periodic domains, such as the FNO [32]. The forcing term poses challenges based upon spatially heterogeneous dynamics. Firstly, this allows us to see if the prediction methods can successfully learn to predict in the presence of heterogeneity. Secondly, this permits us to use the spatially varying random field as a target for inverse inference.

Initial conditions \mathbf{v}_0 and inhomogeneous forcing parameters \mathbf{u} are each drawn from isotropic Gaussian random fields with truncated power-law decay τ of the power spectral density and scale σ , where $\tau_{\mathbf{v}_0} = -3, \sigma_{\mathbf{v}_0} = 0.15, \tau_{\mathbf{u}} = -1, \sigma_{\mathbf{u}} = 0.4$. The variation in the resulting field is due to the alteration in the random seed. We set the domain to the unit square $\Omega = [0, 1]^2$, the viscosity to $\nu = 0.01$. Simulations are implemented using Phiflow [18]. Boundary conditions are Dirichlet, clamping field velocity to null at the perimeter.

D.7 2D Shallow-Water Equations

The shallow-water equations, derived from the general Navier-Stokes equations, present a suitable framework for modelling free-surface flow problems. In 2D, these come in the form of the following system of hyperbolic PDEs,

$$\partial_t h + \partial_x hu + \partial_y hv = 0, \quad (20a)$$

$$\partial_t hu + \partial_x \left(u^2 h + \frac{1}{2} g_r h^2 \right) + \partial_y uvh = -g_r h \partial_x b, \quad (20b)$$

$$\partial_t hv + \partial_y \left(v^2 h + \frac{1}{2} g_r h^2 \right) + \partial_x uvh = -g_r h \partial_y b, \quad (20c)$$

with u, v being the velocities in horizontal and vertical direction, h describing the water depth and b describing a spatially varying bathymetry. hu, hv can be interpreted as the directional momentum components and g_r describes the gravitational acceleration.

The specific simulation we include in our benchmark for the shallow-water equations problem as introduced in D.7 is a 2D radial dam break scenario. On a square domain $\Omega = [-2.5, 2.5]^2$ we initialize the water height as a circular bump in the center of the domain

$$h(t=0, x, y) = \begin{cases} 2.0, & \text{for } r < \sqrt{x^2 + y^2} \\ 1.0, & \text{for } r \geq \sqrt{x^2 + y^2} \end{cases} \quad (21)$$

with the radius r randomly sampled from $\mathcal{U}(0.3, 0.7)$. For generating the datasets we simulate this problem using the PyClaw [23] Python package which offers a comprehensive finite volume solver. A time evolution visualization of the equation is shown in Figure 9.

D.8 Diffusion-Sorption Equation

The diffusion-sorption equation models a diffusion process which is retarded by a sorption process. The equation is written as

$$\partial_t u(t, x) = D/R(u) \partial_{xx} u(t, x), \quad x \in (0, 1), t \in (0, 500]. \quad (22)$$

where D is the effective diffusion coefficient, R is the retardation factor representing the sorption that hinders the diffusion process. Note that R is dependent on the variable u . This equation is applicable to real world scenarios, one of the most prominent being groundwater contaminant transport.

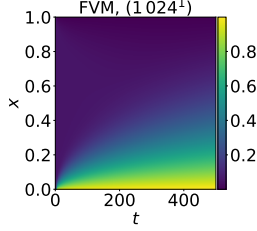


Figure 10: Visualization of the time evolution of the 1D diffusion-sorption equations data.

This equation is retarded by the retardation factor R which is dependent on u based on the Freundlich sorption isotherm [33]:

$$R(u) = 1 + \frac{1 - \phi}{\phi} \rho_s k n_f u^{n_f - 1}, \quad (23)$$

where $\phi = 0.29$ is the porosity of the porous medium, $\rho_s = 2880$ is the bulk density, $k = 3.5 \times 10^{-4}$ is the Freundlich's parameter, $n_f = 0.874$ is the Freundlich's exponent, and the effective diffusion coefficient $D = 5 \times 10^{-4}$. The initial condition is generated with a uniform distribution $u(0, x) \sim U(0, 0.2)$ for $x \in (0, 1)$. We provide datasets discretized into $N_x = 1024$ and $N_t = 501$, as well as the temporally downsampled version for the models training with $N_t = 101$. The spatial discretization is performed using the finite volume method [39] and the time integration using the built-in fourth order Runge-Kutta method in the *scipy* package [60].

This particular example is interesting because of a few things. First, the diffusion coefficient becomes non-linear with dependency on u . And based on Equation 23, it is clear that there is a singularity when $u = 0$. Second, it is highly applicable to a real-world problem, namely the groundwater contaminant transport [41]. To date, application of machine learning to real-world physics problems is still rare. Third, we employ boundary conditions that are not the usual zero or periodic conditions that can be easily padded in models with a convolutional structure. Here, we use $u(t, 0) = 1.0$ and $u(t, 1) = D \partial_x u(t, 1)$. The second boundary condition is particularly challenging since it uses a derivative instead of a constant value. For generating the datasets we simulate this problem using a standard finite volume solver. A time evolution visualization of the equation is shown in Figure 10.

D.9 2D Diffusion-Reaction Equation

In addition to the 1D diffusion-reaction equation, which involves only a single variable, we also consider extending the application to a 2D domain, with two non-linearly coupled variables, namely the activator $u = u(t, x, y)$ and the inhibitor $v = v(t, x, y)$. The equation is written as

$$\partial_t u = D_u \partial_{xx} u + D_u \partial_{yy} u + R_u, \quad \partial_t v = D_v \partial_{xx} v + D_v \partial_{yy} v + R_v, \quad (24)$$

where D_u and D_v are the diffusion coefficient for the activator and inhibitor, respectively, $R_u = R_u(u, v)$ and $R_v = R_v(u, v)$ are the activator and inhibitor reaction function, respectively. The domain of the simulation includes $x \in (-1, 1)$, $y \in (-1, 1)$, $t \in (0, 5]$. This equation is applicable most prominently for modeling biological pattern formation.

The reaction functions for the activator and inhibitor are defined by the Fitzhugh-Nagumo equation [25], written as:

$$R_u(u, v) = u - u^3 - k - v, \quad (25)$$

$$R_v(u, v) = u - v, \quad (26)$$

where $k = 5 \times 10^{-3}$, and the diffusion coefficients for the activator and inhibitor are $D_u = 1 \times 10^{-3}$ and $D_v = 5 \times 10^{-3}$, respectively. The initial condition is generated as standard normal random noise $u(0, x, y) \sim \mathcal{N}(0, 1.0)$ for $x \in (-1, 1)$ and $y \in (-1, 1)$. We provide datasets discretized into $N_x = 512$, $N_y = 512$ and $N_t = 501$, as well as the downsampled version for the models training with $N_x = 128$, $N_y = 128$, and $N_t = 101$. As in the 1D diffusion-sorption equation, the spatial discretization is performed using the finite volume method [39], and the time integration is performed using the built-in fourth order Runge-Kutta method in the *scipy* package [60].

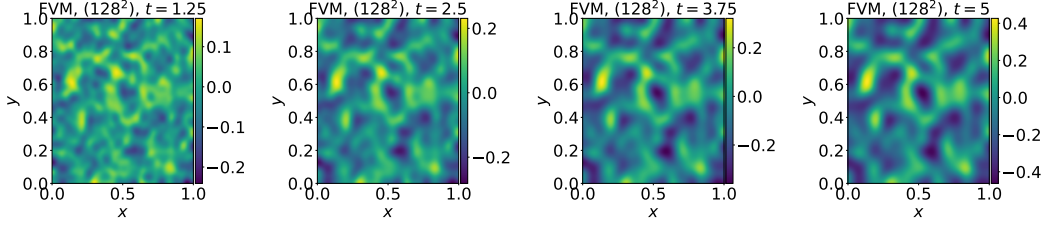


Figure 11: Visualization of the time evolution of the 2D diffusion-reaction equations data.

We included the 2D diffusion-reaction equation as an example because it serves as a challenging benchmark problem. First, there are two variables of interest, namely the activator and inhibitor, which are non-linearly coupled. Second, it also has applicability in real-world problems, namely biological pattern formation [58]. Third, we also employ a no-flow Neumann boundary condition, meaning that $D_u \partial_x u = 0$, $D_v \partial_x v = 0$, $D_u \partial_y u = 0$, and $D_v \partial_y v = 0$ for $x, y \in (-1, 1)^2$. For generating the datasets we simulate this problem using a standard finite volume solver. A time evolution visualization of the equation is shown in Figure 11.

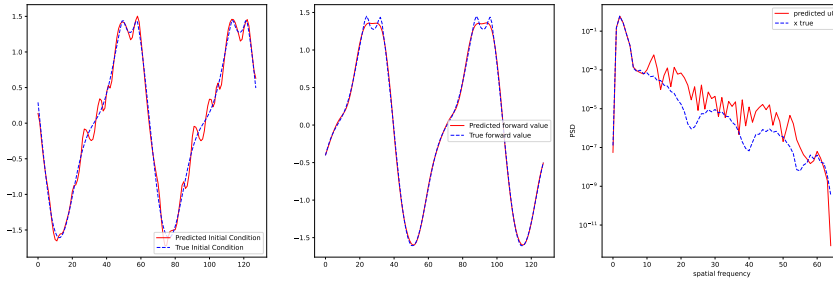


Figure 12: Inverse problem for the 1d advection equation with $\beta = 0.1$. The spectra density where most of the error is concentrated in the higher frequencies is depicted on the right.

D.10 Gradient-Based Inverse Method

The inverse problem aims at solving an inverse inference by minimising the prediction loss[7, 40],

$$\mathcal{L}(u(t = T, x|u_0), u(t = T, x|\hat{u}_0))$$

where $\hat{u}_0 \sim p_\theta(u_0|u(t = T, x))$.

The generation process $p_\theta(u_0|u(t = T, x))$ is a deterministic function, whose parameters θ use a bilinear interpolation to recover the initial condition [35].

Figure 12 shows the solution of the inverse problem for the 1d advection equation. On the left, we see the true and estimated initial condition, and on the right the power density in the frequency domain. As we can see, the error is concentrated in the mid-high frequencies. In the middle we have the true and predicted value at time $t = T$. The error is smaller than in the plot on the left.

Table 2, Table 3 and Table 4 show the error in the spatial and frequency domain of 4 datasets and using FNO and U-Net as surrogate models. In Fig.12, the left figure visualizes the true and the estimated initial condition, while the middle figure is the predicted and the true value. As shown in the figure on the right, the largest error is in the higher frequencies. This effect is also visible from the frequency metrics of Tab.3 and Tab.4. In the experiment we use the same initial and boundary conditions of the forward problem.

| PDE | Metric | Forward model | |
|-------------------|--------|---|---|
| | | FNO | U-Net |
| Advection_beta4 | MSE | $2.4 \times 10^{-3} \pm 3.4 \times 10^{-3}$ | $1.0 \times 10^{+0} \pm 5.6 \times 10^{-2}$ |
| | nL2 | $3.9 \times 10^{-2} \pm 2.9 \times 10^{-2}$ | $1.0 \times 10^{+0} \pm 2.8 \times 10^{-2}$ |
| | nL3 | $4.4 \times 10^{-2} \pm 3.3 \times 10^{-2}$ | $1.0 \times 10^{+0} \pm 2.9 \times 10^{-2}$ |
| | MSE' | $2.9 \times 10^{-4} \pm 5.8 \times 10^{-4}$ | $9.9 \times 10^{-1} \pm 2.5 \times 10^{-2}$ |
| | nL2' | $1.4 \times 10^{-2} \pm 1.1 \times 10^{-2}$ | $1.0 \times 10^{+0} \pm 8.0 \times 10^{-3}$ |
| | nL3' | $1.6 \times 10^{-2} \pm 1.3 \times 10^{-2}$ | $1.0 \times 10^{+0} \pm 8.4 \times 10^{-3}$ |
| Burgers_Nu1 | MSE | $1.0 \times 10^{+0} \pm 2.2 \times 10^{-1}$ | $1.3 \times 10^{+0} \pm 2.3 \times 10^{-1}$ |
| | nL2 | $1.0 \times 10^{+0} \pm 1.0 \times 10^{-1}$ | $1.1 \times 10^{+0} \pm 1.0 \times 10^{-1}$ |
| | nL3 | $1.0 \times 10^{+0} \pm 1.0 \times 10^{-1}$ | $1.1 \times 10^{+0} \pm 1.1 \times 10^{-1}$ |
| | MSE' | $1.3 \times 10^{-4} \pm 2.8 \times 10^{-4}$ | $2.5 \times 10^{-3} \pm 1.9 \times 10^{-3}$ |
| | nL2' | $7.0 \times 10^{-1} \pm 4.6 \times 10^{-1}$ | $1.6 \times 10^{+1} \pm 2.0 \times 10^{+1}$ |
| | nL3' | $7.0 \times 10^{-1} \pm 4.4 \times 10^{-1}$ | $1.7 \times 10^{+1} \pm 2.1 \times 10^{+1}$ |
| CFD_Shock_Trans | MSE | $3.4 \times 10^{+0} \pm 5.3 \times 10^{-1}$ | $1.1 \times 10^{+2} \pm 2.0 \times 10^{+1}$ |
| | nL2 | $1.8 \times 10^{+0} \pm 1.4 \times 10^{-1}$ | $1.0 \times 10^{+1} \pm 1.1 \times 10^{+0}$ |
| | nL3 | $1.9 \times 10^{+0} \pm 2.7 \times 10^{-1}$ | $1.1 \times 10^{+1} \pm 1.6 \times 10^{+0}$ |
| | MSE' | $1.0 \times 10^{-1} \pm 5.9 \times 10^{-2}$ | $4.2 \times 10^{-1} \pm 9.2 \times 10^{-1}$ |
| | nL2' | $3.3 \times 10^{-1} \pm 8.5 \times 10^{-2}$ | $5.8 \times 10^{-1} \pm 3.9 \times 10^{-1}$ |
| | nL3' | $3.6 \times 10^{-1} \pm 9.6 \times 10^{-2}$ | $6.0 \times 10^{-1} \pm 4.0 \times 10^{-1}$ |
| ReacDiff_Nu1_Rho2 | MSE | $1.7 \times 10^{+0} \pm 2.1 \times 10^{-1}$ | $2.0 \times 10^{+0} \pm 3.8 \times 10^{-1}$ |
| | nL2 | $1.3 \times 10^{+0} \pm 8.4 \times 10^{-2}$ | $1.4 \times 10^{+0} \pm 1.3 \times 10^{-1}$ |
| | nL3 | $1.3 \times 10^{+0} \pm 8.1 \times 10^{-2}$ | $1.5 \times 10^{+0} \pm 1.3 \times 10^{-1}$ |
| | MSE' | $5.4 \times 10^{-2} \pm 1.2 \times 10^{-1}$ | $6.4 \times 10^{-1} \pm 3.5 \times 10^{-1}$ |
| | nL2' | $1.2 \times 10^{-1} \pm 1.2 \times 10^{-1}$ | $7.3 \times 10^{-1} \pm 5.1 \times 10^{-2}$ |
| | nL3' | $1.2 \times 10^{-1} \pm 1.2 \times 10^{-1}$ | $7.3 \times 10^{-1} \pm 5.0 \times 10^{-2}$ |

Table 2: Error of the inverse problem. The prime indicates the error of the prediction, for example MSE' is the MSE at time $t = T$. The MSE for example in the first row is one order of magnitude lower. nL2 and nL3 are the normalized L2 and L3 norm error, $nLp = \|\hat{\mathbf{y}} - \mathbf{y}\|_p / \|\mathbf{y}\|_p, p = 2, 3$.

| PDE | Metric | Forward model | |
|-------------------|------------|-----------------------|-----------------------|
| | | FNO | U-Net |
| Advection_beta4 | fMSE | 3.04×10^{-1} | $1.29 \times 10^{+2}$ |
| | fMSE low | 5.56×10^{-1} | $1.29 \times 10^{+2}$ |
| | fMSE mid | 5.26×10^{-2} | $1.29 \times 10^{+2}$ |
| | fMSE high | 3.03×10^{-1} | $1.29 \times 10^{+2}$ |
| | fMSE' | 3.67×10^{-2} | 9.92×10^{-1} |
| | fMSE' low | 1.60×10^{-2} | 9.92×10^{-1} |
| | fMSE' mid | 5.74×10^{-2} | 9.92×10^{-1} |
| | fMSE' high | 3.68×10^{-2} | 9.92×10^{-1} |
| | fL2 | 3.91×10^{-2} | $1.00 \times 10^{+0}$ |
| | fL2 low | 3.75×10^{-2} | $1.01 \times 10^{+0}$ |
| | fL2 mid | $1.41 \times 10^{+1}$ | $0.00 \times 10^{+0}$ |
| | fL2 high | 3.90×10^{-2} | $0.00 \times 10^{+0}$ |
| Burgers_Nu1 | fMSE | $1.29 \times 10^{+2}$ | $1.59 \times 10^{+2}$ |
| | fMSE low | $2.58 \times 10^{+2}$ | $1.59 \times 10^{+2}$ |
| | fMSE mid | 1.19×10^{-1} | $1.59 \times 10^{+2}$ |
| | fMSE high | $1.29 \times 10^{+2}$ | $1.59 \times 10^{+2}$ |
| | fMSE' | 1.67×10^{-2} | 2.46×10^{-3} |
| | fMSE' low | 3.36×10^{-2} | 2.46×10^{-3} |
| | fMSE' mid | 9.26×10^{-7} | 2.46×10^{-3} |
| | fMSE' high | 1.66×10^{-2} | 2.46×10^{-3} |
| | fL2 | 9.98×10^{-1} | $1.11 \times 10^{+0}$ |
| | fL2 low | 9.98×10^{-1} | $1.11 \times 10^{+0}$ |
| | fL2 mid | $3.50 \times 10^{+0}$ | $0.00 \times 10^{+0}$ |
| | fL2 high | 9.98×10^{-1} | $0.00 \times 10^{+0}$ |
| CFD_Shock_Trans | fMSE | $4.37 \times 10^{+2}$ | $1.40 \times 10^{+4}$ |
| | fMSE low | $4.37 \times 10^{+2}$ | $1.40 \times 10^{+4}$ |
| | fMSE mid | $4.37 \times 10^{+2}$ | $1.40 \times 10^{+4}$ |
| | fMSE high | $4.37 \times 10^{+2}$ | $1.40 \times 10^{+4}$ |
| | fMSE' | $1.28 \times 10^{+1}$ | $2.19 \times 10^{+2}$ |
| | fMSE' low | $3.21 \times 10^{+1}$ | $2.19 \times 10^{+2}$ |
| | fMSE' mid | $1.13 \times 10^{+0}$ | $2.19 \times 10^{+2}$ |
| | fMSE' high | $8.98 \times 10^{+0}$ | $2.19 \times 10^{+2}$ |
| | fL2 | $1.84 \times 10^{+0}$ | $1.04 \times 10^{+1}$ |
| | fL2 low | $1.51 \times 10^{+0}$ | $9.95 \times 10^{+0}$ |
| | fL2 mid | $0.00 \times 10^{+0}$ | $0.00 \times 10^{+0}$ |
| | fL2 high | $0.00 \times 10^{+0}$ | $0.00 \times 10^{+0}$ |
| ReacDiff_Nu1_Rho2 | fMSE | $2.17 \times 10^{+2}$ | $2.55 \times 10^{+2}$ |
| | fMSE low | $6.10 \times 10^{+2}$ | $2.55 \times 10^{+2}$ |
| | fMSE mid | 1.48×10^{-2} | $2.55 \times 10^{+2}$ |
| | fMSE high | $1.28 \times 10^{+2}$ | $2.55 \times 10^{+2}$ |
| | fMSE' | $6.94 \times 10^{+0}$ | 6.35×10^{-1} |
| | fMSE' low | $2.77 \times 10^{+1}$ | 6.35×10^{-1} |
| | fMSE' mid | 1.14×10^{-5} | 6.35×10^{-1} |
| | fMSE' high | 1.29×10^{-4} | 6.35×10^{-1} |
| | fL2 | $1.30 \times 10^{+0}$ | $1.41 \times 10^{+0}$ |
| | fL2 low | $1.54 \times 10^{+0}$ | $1.60 \times 10^{+0}$ |
| | fL2 mid | $7.45 \times 10^{+0}$ | $0.00 \times 10^{+0}$ |
| | fL2 high | $1.00 \times 10^{+0}$ | $0.00 \times 10^{+0}$ |

Table 3: Frequency error of the inverse problem. fMSE, fL2 and fL3 are the frequency version of the MSE, normalized L2 and L3 norm metrics. Low, mid and high is the range of frequencies. Prime is used for the error in the prediction, without the error of the initial condition estimation. Normalised metric are not well defined, when the original signal is zero.

| PDE | Metric | Forward model | |
|-------------------|-----------|------------------------|------------------------|
| | | FNO | U-Net |
| Advection_beta4 | fL2' | 1.36×10^{-2} | $1.13 \times 10^{+1}$ |
| | fL2' low | 7.50×10^{-3} | $5.66 \times 10^{+0}$ |
| | fL2' mid | $1.61 \times 10^{+0}$ | $5.27 \times 10^{+1}$ |
| | fL2' high | 1.36×10^{-2} | $8.01 \times 10^{+0}$ |
| | fL3 | 3.14×10^{-2} | $1.00 \times 10^{+0}$ |
| | fL3 low | 3.12×10^{-2} | $1.00 \times 10^{+0}$ |
| | fL3 mid | $1.75 \times 10^{+1}$ | $0.00 \times 10^{+0}$ |
| | fL3 high | 3.14×10^{-2} | $0.00 \times 10^{+0}$ |
| | fL3' | 9.51×10^{-3} | $5.04 \times 10^{+0}$ |
| | fL3' low | 5.62×10^{-3} | $3.18 \times 10^{+0}$ |
| | fL3' mid | $1.47 \times 10^{+0}$ | $2.77 \times 10^{+1}$ |
| | fL3' high | 9.51×10^{-3} | $4.00 \times 10^{+0}$ |
| Burgers_Nu1 | fL2' | 7.00×10^{-1} | $1.82 \times 10^{+2}$ |
| | fL2' low | 7.99×10^{-1} | $6.28 \times 10^{+1}$ |
| | fL2' mid | $1.03 \times 10^{+2}$ | $5.84 \times 10^{+5}$ |
| | fL2' high | 5.39×10^{-1} | $1.31 \times 10^{+2}$ |
| | fL3 | 9.97×10^{-1} | $1.04 \times 10^{+0}$ |
| | fL3 low | 9.97×10^{-1} | $1.04 \times 10^{+0}$ |
| | fL3 mid | $3.58 \times 10^{+0}$ | $0.00 \times 10^{+0}$ |
| | fL3 high | 9.97×10^{-1} | $0.00 \times 10^{+0}$ |
| | fL3' | 7.21×10^{-1} | $4.88 \times 10^{+1}$ |
| | fL3' low | 7.99×10^{-1} | $2.40 \times 10^{+1}$ |
| | fL3' mid | $9.35 \times 10^{+1}$ | $2.98 \times 10^{+5}$ |
| | fL3' high | 5.39×10^{-1} | $3.92 \times 10^{+1}$ |
| CFD_Shock_Trans | fL2' | 3.34×10^{-1} | $2.12 \times 10^{+0}$ |
| | fL2' low | 2.68×10^{-1} | $2.14 \times 10^{+0}$ |
| | fL2' mid | $0.00 \times 10^{+0}$ | $0.00 \times 10^{+0}$ |
| | fL2' high | $0.00 \times 10^{+0}$ | $0.00 \times 10^{+0}$ |
| | fL3 | $1.26 \times 10^{+0}$ | $9.41 \times 10^{+0}$ |
| | fL3 low | $1.11 \times 10^{+0}$ | $9.36 \times 10^{+0}$ |
| | fL3 mid | $0.00 \times 10^{+0}$ | $0.00 \times 10^{+0}$ |
| | fL3 high | $0.00 \times 10^{+0}$ | $0.00 \times 10^{+0}$ |
| | fL3' | 2.16×10^{-1} | $2.19 \times 10^{+0}$ |
| | fL3' low | 1.96×10^{-1} | $2.20 \times 10^{+0}$ |
| | fL3' mid | $0.00 \times 10^{+0}$ | $0.00 \times 10^{+0}$ |
| | fL3' high | $0.00 \times 10^{+0}$ | $0.00 \times 10^{+0}$ |
| ReacDiff_Nu1_Rho2 | fL2' | 1.23×10^{-1} | $1.18 \times 10^{+1}$ |
| | fL2' low | 1.23×10^{-1} | $5.83 \times 10^{+0}$ |
| | fL2' mid | $1.89 \times 10^{+18}$ | $1.90 \times 10^{+21}$ |
| | fL2' high | $9.03 \times 10^{+18}$ | $3.93 \times 10^{+21}$ |
| | fL3 | $1.27 \times 10^{+0}$ | $1.29 \times 10^{+0}$ |
| | fL3 low | $1.45 \times 10^{+0}$ | $1.47 \times 10^{+0}$ |
| | fL3 mid | $7.07 \times 10^{+0}$ | $0.00 \times 10^{+0}$ |
| | fL3 high | $1.00 \times 10^{+0}$ | $0.00 \times 10^{+0}$ |
| | fL3' | 1.23×10^{-1} | $5.08 \times 10^{+0}$ |
| | fL3' low | 1.23×10^{-1} | $3.18 \times 10^{+0}$ |
| | fL3' mid | $1.07 \times 10^{+18}$ | $7.25 \times 10^{+20}$ |
| | fL3' high | $6.54 \times 10^{+18}$ | $1.14 \times 10^{+21}$ |

Table 4: Frequency error of the prediction of the inverse problem. fMSE, fL2 and fL3 are the frequency version of the MSE, normalized L2 and L3 norm metrics. Low, mid and high is the range of the frequencies. Prime is used for the error in the prediction, without the error of the initial condition estimation. Normalised metric are not well defined, when the original signal is zero.

E Detailed Baseline Score

Table 5: Summary of the baseline models’ performance for different evaluation metrics: RMSE, normalised RMSE (nRMSE), RMSE from conserved value (cRMSE), maximum error, RMSE at the boundaries (bRMSE), RMSE in Fourier space at low (fRMSE low), medium (fRMSE mid), and high frequency (fRMSE high) ranges applied to the diffusion-sorption, 2D diffusion-reaction, and shallow-water equations.

| PDE | Parameter | Metric | Baseline model | | |
|------------------------|-----------|------------|----------------------|----------------------|----------------------|
| | | | U-Net | FNO | PINN |
| Diffusion-sorption | N/A | RMSE | 5.8×10^{-2} | 5.9×10^{-4} | 9.9×10^{-2} |
| | | nRMSE | 1.5×10^{-1} | 1.7×10^{-3} | 2.2×10^{-1} |
| | | max error | 2.9×10^{-1} | 7.8×10^{-3} | 2.2×10^{-1} |
| | | cRMSE | 4.8×10^{-2} | 1.9×10^{-4} | 7.5×10^{-2} |
| | | bRMSE | 6.1×10^{-3} | 2.0×10^{-3} | 1.4×10^{-1} |
| | | fRMSE low | 1.9×10^{-2} | 1.5×10^{-4} | 3.5×10^{-2} |
| | | fRMSE mid | 4.7×10^{-3} | 5.0×10^{-5} | 5.2×10^{-3} |
| | | fRMSE high | 1.9×10^{-4} | 7.1×10^{-6} | 2.7×10^{-4} |
| 2D diffusion-reaction | N/A | RMSE | 6.1×10^{-2} | 8.1×10^{-3} | 1.9×10^{-1} |
| | | nRMSE | 8.4×10^{-1} | 1.2×10^{-1} | $1.6 \times 10^{+0}$ |
| | | max error | 1.9×10^{-1} | 9.1×10^{-2} | 5.0×10^{-1} |
| | | cRMSE | 3.9×10^{-2} | 1.7×10^{-3} | 1.3×10^{-1} |
| | | bRMSE | 7.8×10^{-2} | 2.7×10^{-2} | 2.2×10^{-1} |
| | | fRMSE low | 1.7×10^{-2} | 8.2×10^{-4} | 5.7×10^{-2} |
| | | fRMSE mid | 5.4×10^{-3} | 7.7×10^{-4} | 1.3×10^{-2} |
| | | fRMSE high | 6.8×10^{-4} | 4.1×10^{-4} | 1.5×10^{-3} |
| Shallow-water equation | N/A | RMSE | 8.6×10^{-2} | 4.5×10^{-3} | 1.7×10^{-2} |
| | | nRMSE | 8.3×10^{-2} | 4.4×10^{-3} | 1.7×10^{-2} |
| | | max error | 4.4×10^{-1} | 4.5×10^{-2} | 1.3×10^{-3} |
| | | cRMSE | 1.3×10^{-2} | 2.0×10^{-4} | 1.7×10^{-2} |
| | | bRMSE | 4.2×10^{-3} | 1.4×10^{-3} | 1.5×10^{-1} |
| | | fRMSE low | 2.0×10^{-2} | 2.6×10^{-4} | 5.9×10^{-3} |
| | | fRMSE mid | 7.0×10^{-3} | 3.1×10^{-4} | 1.9×10^{-3} |
| | | fRMSE high | 8.6×10^{-4} | 2.5×10^{-4} | 6.0×10^{-4} |

Table 6: Summary of the baseline models' performance for different evaluation metrics: RMSE, normalised RMSE (nRMSE), RMSE from conserved value (cRMSE), maximum error, RMSE at the boundaries (bRMSE), RMSE in Fourier space at low (fRMSE low), medium (fRMSE mid), and high frequency (fRMSE high) ranges applied to the advection equation with different parameter values.

| PDE | Parameter | Metric | Baseline model | | |
|---------------|---------------|----------------------|----------------------|----------------------|----------------------|
| | | | U-Net | FNO | PINN |
| Advection | $\beta = 0.1$ | RMSE | 3.1×10^{-2} | 4.1×10^{-3} | 6.7×10^{-3} |
| | | nRMSE | 5.0×10^{-2} | 7.7×10^{-3} | 7.8×10^{-3} |
| | | max error | 5.1×10^{-1} | 1.1×10^{-1} | 2.0×10^{-2} |
| | | cRMSE | 1.5×10^{-2} | 3.8×10^{-4} | 1.5×10^{-3} |
| | | bRMSE | 6.6×10^{-2} | 4.0×10^{-3} | 1.7×10^{-2} |
| | | fRMSE low | 8.7×10^{-2} | 3.5×10^{-4} | 2.2×10^{-3} |
| | | fRMSE mid | 4.5×10^{-3} | 4.4×10^{-4} | 3.9×10^{-4} |
| | | fRMSE high | 9.5×10^{-4} | 2.4×10^{-4} | 4.8×10^{-6} |
| | $\beta = 0.4$ | RMSE | 1.5×10^{-1} | 5.3×10^{-3} | 2.6×10^{-2} |
| | | nRMSE | 2.3×10^{-1} | 1.0×10^{-2} | 3.0×10^{-2} |
| | | max error | 8.8×10^{-1} | 1.6×10^{-1} | 7.0×10^{-2} |
| | | cRMSE | 6.1×10^{-2} | 4.2×10^{-4} | 7.7×10^{-3} |
| | | bRMSE | 1.4×10^{-1} | 4.6×10^{-3} | 3.9×10^{-2} |
| | | fRMSE low | 5.5×10^{-2} | 4.3×10^{-4} | 6.6×10^{-3} |
| | | fRMSE mid | 1.3×10^{-2} | 4.5×10^{-4} | 3.3×10^{-3} |
| | | fRMSE high | 1.0×10^{-3} | 3.1×10^{-4} | 2.6×10^{-5} |
| | $\beta = 1.0$ | RMSE | 1.4×10^{-1} | 5.2×10^{-3} | 1.1×10^{-2} |
| | | nRMSE | 2.3×10^{-1} | 9.7×10^{-3} | 1.3×10^{-2} |
| | | max error | 9.5×10^{-1} | 2.0×10^{-1} | 2.0×10^{-2} |
| | | cRMSE | 5.2×10^{-2} | 4.5×10^{-4} | 2.7×10^{-3} |
| bRMSE | | 1.4×10^{-1} | 4.6×10^{-3} | 8.3×10^{-3} | |
| fRMSE low | | 5.7×10^{-2} | 3.5×10^{-4} | 3.0×10^{-3} | |
| fRMSE mid | | 1.3×10^{-2} | 3.7×10^{-4} | 9.4×10^{-4} | |
| fRMSE high | | 9.8×10^{-4} | 3.0×10^{-4} | 4.8×10^{-6} | |
| $\beta = 4.0$ | RMSE | 1.3×10^{-2} | 3.9×10^{-3} | 6.6×10^{-1} | |
| | nRMSE | 2.4×10^{-2} | 6.7×10^{-3} | 7.7×10^{-1} | |
| | max error | 1.3×10^{-1} | 9.0×10^{-2} | $1.0 \times 10^{+0}$ | |
| | cRMSE | 4.1×10^{-3} | 2.4×10^{-4} | 1.8×10^{-2} | |
| | bRMSE | 2.4×10^{-2} | 3.1×10^{-3} | 4.9×10^{-1} | |
| | fRMSE low | 3.6×10^{-3} | 3.0×10^{-4} | 1.5×10^{-1} | |
| | fRMSE mid | 1.7×10^{-3} | 3.0×10^{-4} | 2.1×10^{-4} | |
| | fRMSE high | 3.9×10^{-4} | 2.2×10^{-4} | 7.2×10^{-6} | |

Table 7: Summary of the baseline models’ performance for different evaluation metrics: RMSE, normalised RMSE (nRMSE), RMSE from conserved value (cRMSE), maximum error, RMSE at the boundaries (bRMSE), RMSE in Fourier space at low (fRMSE low), medium (fRMSE mid), and high frequency (fRMSE high) ranges applied to the Burgers’ equation with different parameter values.

| PDE | Parameter | Metric | Baseline model | | |
|------------|---------------|----------------------|----------------------|----------------------|----------------------|
| | | | U-Net | FNO | PINN |
| Burgers’ | $\nu = 0.001$ | RMSE | 1.3×10^{-1} | 9.6×10^{-3} | 2.2×10^{-1} |
| | | nRMSE | 3.7×10^{-1} | 2.9×10^{-2} | 3.9×10^{-1} |
| | | max error | 6.0×10^{-1} | 2.3×10^{-1} | 4.3×10^{-1} |
| | | cRMSE | 8.5×10^{-2} | 8.6×10^{-4} | 1.3×10^{-1} |
| | | bRMSE | 1.2×10^{-1} | 9.1×10^{-3} | 2.1×10^{-1} |
| | | fRMSE low | 4.6×10^{-2} | 8.5×10^{-4} | 7.8×10^{-2} |
| | | fRMSE mid | 1.1×10^{-2} | 1.1×10^{-3} | 1.1×10^{-2} |
| | | fRMSE high | 1.5×10^{-3} | 5.1×10^{-4} | 2.7×10^{-4} |
| | $\nu = 0.01$ | RMSE | 7.0×10^{-2} | 2.7×10^{-3} | 4.7×10^{-1} |
| | | nRMSE | 2.2×10^{-1} | 7.8×10^{-3} | 8.5×10^{-1} |
| | | max error | 4.6×10^{-1} | 6.4×10^{-2} | 6.8×10^{-1} |
| | | cRMSE | 2.7×10^{-2} | 5.0×10^{-4} | 4.7×10^{-1} |
| | | bRMSE | 7.1×10^{-2} | 4.0×10^{-3} | 6.8×10^{-1} |
| | | fRMSE low | 2.6×10^{-2} | 5.3×10^{-4} | 1.3×10^{-1} |
| | | fRMSE mid | 7.1×10^{-3} | 4.7×10^{-4} | 7.9×10^{-3} |
| | | fRMSE high | 4.9×10^{-4} | 8.7×10^{-5} | 6.7×10^{-5} |
| | $\nu = 0.1$ | RMSE | 4.6×10^{-2} | 7.6×10^{-4} | 2.5×10^{-1} |
| | | nRMSE | 2.3×10^{-1} | 2.9×10^{-3} | 4.6×10^{-1} |
| | | max error | 2.9×10^{-1} | 9.6×10^{-3} | 3.3×10^{-1} |
| | | cRMSE | 2.5×10^{-2} | 2.2×10^{-4} | 2.4×10^{-1} |
| | | bRMSE | 6.2×10^{-2} | 1.1×10^{-3} | 2.4×10^{-1} |
| | | fRMSE low | 1.8×10^{-2} | 3.1×10^{-4} | 7.1×10^{-2} |
| | | fRMSE mid | 2.8×10^{-3} | 6.7×10^{-5} | 1.2×10^{-4} |
| | | fRMSE high | 8.3×10^{-4} | 8.5×10^{-6} | 4.4×10^{-6} |
| | $\nu = 1.0$ | RMSE | 2.7×10^{-2} | 1.2×10^{-3} | 1.1×10^{-2} |
| | | nRMSE | 2.4×10^{-1} | 4.0×10^{-3} | 1.9×10^{-2} |
| | | max error | 1.7×10^{-1} | 8.0×10^{-3} | 1.6×10^{-2} |
| | | cRMSE | 1.7×10^{-2} | 1.1×10^{-4} | 9.6×10^{-3} |
| bRMSE | | 2.6×10^{-2} | 1.2×10^{-3} | 5.6×10^{-3} | |
| fRMSE low | | 1.0×10^{-2} | 4.2×10^{-4} | 3.2×10^{-3} | |
| fRMSE mid | | 1.8×10^{-3} | 1.6×10^{-5} | 6.0×10^{-5} | |
| fRMSE high | | 2.3×10^{-4} | 1.5×10^{-6} | 3.2×10^{-6} | |

Table 8: Summary of the baseline models' performance for different evaluation metrics: RMSE, normalised RMSE (nRMSE), RMSE from conserved value (cRMSE), maximum error, RMSE at the boundaries (bRMSE), RMSE in Fourier space at low (fRMSE low), medium (fRMSE mid), and high frequency (fRMSE high) ranges applied to the Darcy flow equation with different parameter values.

| PDE | Parameter | Metric | Baseline model | |
|-----------------|----------------|----------------------|----------------------|----------------------|
| | | | U-Net | FNO |
| DarcyFlow | $\beta = 0.01$ | RMSE | 4.0×10^{-3} | 8.0×10^{-3} |
| | | nRMSE | $1.1 \times 10^{+0}$ | $2.5 \times 10^{+0}$ |
| | | max error | 6.8×10^{-2} | 1.5×10^{-1} |
| | | cRMSE | 5.8×10^{-3} | 1.3×10^{-2} |
| | | bRMSE | 6.3×10^{-4} | 4.7×10^{-3} |
| | | fRMSE low | 2.5×10^{-3} | 5.2×10^{-3} |
| | | fRMSE mid | 1.3×10^{-4} | 1.5×10^{-4} |
| | | fRMSE high | 2.1×10^{-5} | 1.6×10^{-5} |
| | $\beta = 0.1$ | RMSE | 4.8×10^{-3} | 6.2×10^{-3} |
| | | nRMSE | 1.8×10^{-1} | 2.2×10^{-1} |
| | | max error | 7.0×10^{-2} | 8.9×10^{-2} |
| | | cRMSE | 6.0×10^{-3} | 7.7×10^{-3} |
| | | bRMSE | 8.6×10^{-4} | 5.0×10^{-3} |
| | | fRMSE low | 2.6×10^{-3} | 3.6×10^{-3} |
| | | fRMSE mid | 1.9×10^{-4} | 2.6×10^{-4} |
| | | fRMSE high | 4.4×10^{-5} | 4.5×10^{-5} |
| | $\beta = 1.0$ | RMSE | 6.4×10^{-3} | 1.2×10^{-2} |
| | | nRMSE | 3.3×10^{-2} | 6.4×10^{-2} |
| | | max error | 9.0×10^{-2} | 1.1×10^{-1} |
| | | cRMSE | 6.0×10^{-3} | 1.1×10^{-2} |
| bRMSE | | 3.5×10^{-3} | 5.5×10^{-3} | |
| fRMSE low | | 3.0×10^{-3} | 5.2×10^{-3} | |
| fRMSE mid | | 3.4×10^{-4} | 5.1×10^{-4} | |
| fRMSE high | | 1.3×10^{-4} | 1.5×10^{-4} | |
| $\beta = 10.0$ | RMSE | 1.4×10^{-2} | 2.1×10^{-2} | |
| | nRMSE | 8.2×10^{-3} | 1.2×10^{-2} | |
| | max error | 2.4×10^{-1} | 3.2×10^{-1} | |
| | cRMSE | 9.9×10^{-3} | 1.5×10^{-2} | |
| | bRMSE | 9.4×10^{-3} | 1.6×10^{-2} | |
| | fRMSE low | 5.8×10^{-3} | 8.3×10^{-3} | |
| | fRMSE mid | 9.8×10^{-4} | 1.3×10^{-3} | |
| | fRMSE high | 3.6×10^{-4} | 5.7×10^{-4} | |
| $\beta = 100.0$ | RMSE | 7.3×10^{-2} | 1.1×10^{-1} | |
| | nRMSE | 4.4×10^{-3} | 6.4×10^{-3} | |
| | max error | $1.7 \times 10^{+0}$ | $2.1 \times 10^{+0}$ | |
| | cRMSE | 5.1×10^{-2} | 8.9×10^{-2} | |
| | bRMSE | 4.6×10^{-2} | 7.9×10^{-2} | |
| | fRMSE low | 2.9×10^{-2} | 4.6×10^{-2} | |
| | fRMSE mid | 5.3×10^{-3} | 7.6×10^{-3} | |
| | fRMSE high | 2.5×10^{-3} | 3.6×10^{-3} | |

Table 9: Summary of the baseline models' performance for different evaluation metrics: RMSE, normalised RMSE (nRMSE), RMSE from conserved value (cRMSE), maximum error, RMSE at the boundaries (bRMSE), RMSE in Fourier space at low (fRMSE low), medium (fRMSE mid), and high frequency (fRMSE high) ranges applied to the 1d diffusion-reaction equation with different parameter values.

| PDE | Parameter | Metric | Baseline model | | |
|------------|--------------------------|----------------------|----------------------|----------------------|----------------------|
| | | | U-Net | FNO | PINN |
| ReacDiff | $\nu = 0.5, \rho = 1.0$ | RMSE | 3.1×10^{-3} | 6.3×10^{-4} | 4.5×10^{-2} |
| | | nRMSE | 6.0×10^{-3} | 1.4×10^{-3} | 8.0×10^{-2} |
| | | max error | 1.8×10^{-2} | 8.7×10^{-3} | 7.6×10^{-2} |
| | | cRMSE | 2.5×10^{-3} | 1.3×10^{-3} | 4.3×10^{-2} |
| | | bRMSE | 3.7×10^{-3} | 6.7×10^{-4} | 7.5×10^{-2} |
| | | fRMSE low | 1.1×10^{-3} | 4.1×10^{-4} | 1.4×10^{-2} |
| | | fRMSE mid | 1.8×10^{-4} | 9.1×10^{-6} | 2.4×10^{-4} |
| | | fRMSE high | 1.8×10^{-5} | 1.7×10^{-6} | 3.7×10^{-6} |
| | $\nu = 0.5, \rho = 10.0$ | RMSE | 6.2×10^{-8} | $0.0 \times 10^{+0}$ | 1.4×10^{-2} |
| | | nRMSE | 6.5×10^{-8} | $0.0 \times 10^{+0}$ | 1.4×10^{-2} |
| | | max error | 6.2×10^{-8} | $0.0 \times 10^{+0}$ | 2.6×10^{-2} |
| | | cRMSE | 6.2×10^{-8} | $0.0 \times 10^{+0}$ | 6.2×10^{-3} |
| | | bRMSE | 6.2×10^{-8} | $0.0 \times 10^{+0}$ | 2.3×10^{-2} |
| | | fRMSE low | 1.6×10^{-8} | $0.0 \times 10^{+0}$ | 4.3×10^{-3} |
| | | fRMSE mid | $0.0 \times 10^{+0}$ | $0.0 \times 10^{+0}$ | 2.5×10^{-4} |
| | | fRMSE high | $0.0 \times 10^{+0}$ | $0.0 \times 10^{+0}$ | 2.9×10^{-6} |
| | $\nu = 2.0, \rho = 1.0$ | RMSE | 2.3×10^{-3} | 2.9×10^{-4} | 3.9×10^{-1} |
| | | nRMSE | 4.5×10^{-3} | 7.0×10^{-4} | 7.3×10^{-1} |
| | | max error | 2.0×10^{-2} | 4.2×10^{-3} | 3.9×10^{-1} |
| | | cRMSE | 1.9×10^{-3} | 6.4×10^{-4} | 3.9×10^{-1} |
| | | bRMSE | 1.8×10^{-3} | 4.1×10^{-4} | 3.9×10^{-1} |
| | | fRMSE low | 7.7×10^{-4} | 1.9×10^{-4} | 9.7×10^{-2} |
| | | fRMSE mid | 1.7×10^{-4} | 9.2×10^{-6} | 6.2×10^{-5} |
| | | fRMSE high | 2.6×10^{-5} | 1.8×10^{-6} | 3.4×10^{-6} |
| | $\nu = 2.0, \rho = 10.0$ | RMSE | 3.1×10^{-8} | 6.2×10^{-8} | 3.2×10^{-2} |
| | | nRMSE | 3.2×10^{-8} | 6.5×10^{-8} | 3.3×10^{-2} |
| | | max error | 3.1×10^{-8} | 6.2×10^{-8} | 3.2×10^{-2} |
| | | cRMSE | 3.1×10^{-8} | 6.2×10^{-8} | 3.2×10^{-2} |
| bRMSE | | 3.1×10^{-8} | 6.2×10^{-8} | 3.1×10^{-2} | |
| fRMSE low | | 7.8×10^{-9} | 1.6×10^{-8} | 8.0×10^{-3} | |
| fRMSE mid | | $0.0 \times 10^{+0}$ | $0.0 \times 10^{+0}$ | 6.4×10^{-6} | |
| fRMSE high | | $0.0 \times 10^{+0}$ | $0.0 \times 10^{+0}$ | 2.7×10^{-7} | |

Table 10: Summary of the baseline models' performance for different evaluation metrics: RMSE, normalised RMSE (nRMSE), RMSE from conserved value (cRMSE), maximum error, RMSE at the boundaries (bRMSE), RMSE in Fourier space at low (fRMSE low), medium (fRMSE mid), and high frequency (fRMSE high) ranges applied to the 1d compressible Navier-Stokes equation with different parameter values.

| PDE | Parameter | Metric | Baseline model | |
|-------------------------|-------------------------------------|----------------------|----------------------|----------------------|
| | | | U-Net | FNO |
| 1DCFD | $\eta = \zeta = 0.01$ Rand periodic | RMSE | 9.9×10^{-1} | 2.7×10^{-1} |
| | | nRMSE | 3.6×10^{-1} | 9.5×10^{-2} |
| | | max error | $7.8 \times 10^{+0}$ | $4.1 \times 10^{+0}$ |
| | | cRMSE | 3.6×10^{-1} | 5.0×10^{-2} |
| | | bRMSE | $1.0 \times 10^{+0}$ | 2.2×10^{-1} |
| | | fRMSE low | 3.6×10^{-1} | 7.3×10^{-2} |
| | | fRMSE mid | 1.2×10^{-1} | 5.5×10^{-2} |
| | | fRMSE high | 9.2×10^{-3} | 3.7×10^{-3} |
| | $\eta = \zeta = 0.1$ Rand periodic | RMSE | 6.6×10^{-1} | 9.3×10^{-2} |
| | | nRMSE | 7.2×10^{-1} | 6.8×10^{-2} |
| | | max error | $5.3 \times 10^{+0}$ | $1.5 \times 10^{+0}$ |
| | | cRMSE | 3.5×10^{-1} | 2.7×10^{-2} |
| bRMSE | | 6.8×10^{-1} | 7.6×10^{-2} | |
| fRMSE low | | 2.5×10^{-1} | 2.8×10^{-2} | |
| fRMSE mid | | 5.7×10^{-2} | 1.3×10^{-2} | |
| fRMSE high | | 7.7×10^{-3} | 2.0×10^{-3} | |
| inviscid Rand periodic | RMSE | $1.7 \times 10^{+1}$ | 4.7×10^{-1} | |
| | nRMSE | $1.1 \times 10^{+0}$ | 1.2×10^{-1} | |
| | max error | $2.0 \times 10^{+1}$ | $7.1 \times 10^{+0}$ | |
| | cRMSE | $1.7 \times 10^{+1}$ | 6.7×10^{-2} | |
| | bRMSE | $1.6 \times 10^{+1}$ | 3.5×10^{-1} | |
| | fRMSE low | 5.3×10^{-1} | $4.5 \times 10^{+0}$ | |
| | fRMSE mid | 1.9×10^{-1} | 1.6×10^{-1} | |
| | fRMSE high | 2.1×10^{-2} | 2.6×10^{-3} | |
| inviscid Rand Outgoing | RMSE | $1.6 \times 10^{+0}$ | 2.6×10^{-1} | |
| | nRMSE | $1.1 \times 10^{+1}$ | $6.7 \times 10^{+0}$ | |
| | max error | $1.2 \times 10^{+1}$ | $4.3 \times 10^{+0}$ | |
| | cRMSE | $1.5 \times 10^{+0}$ | 1.5×10^{-1} | |
| | bRMSE | $1.8 \times 10^{+0}$ | 3.6×10^{-1} | |
| | fRMSE low | 6.8×10^{-1} | 9.0×10^{-2} | |
| | fRMSE mid | 1.2×10^{-1} | 4.5×10^{-2} | |
| | fRMSE high | 1.6×10^{-2} | 6.7×10^{-3} | |
| inviscid Shock Outgoing | RMSE | 4.1×10^{-1} | 1.6×10^{-1} | |
| | nRMSE | 1.7×10^{-1} | 4.7×10^{-2} | |
| | max error | $6.6 \times 10^{+0}$ | $3.8 \times 10^{+0}$ | |
| | cRMSE | 2.1×10^{-1} | 5.3×10^{-2} | |
| | bRMSE | 5.6×10^{-1} | 2.4×10^{-1} | |
| | fRMSE low | 1.4×10^{-1} | 3.7×10^{-2} | |
| | fRMSE mid | 5.3×10^{-2} | 2.6×10^{-2} | |
| | fRMSE high | 1.1×10^{-2} | 6.7×10^{-3} | |

Table 11: Summary of the baseline models' performance for different evaluation metrics: RMSE, normalised RMSE (nRMSE), RMSE from conserved value (cRMSE), maximum error, RMSE at the boundaries (bRMSE), RMSE in Fourier space at low (fRMSE low), medium (fRMSE mid), and high frequency (fRMSE high) ranges applied to the 2d compressible Navier-Stokes equation with different parameter values (first part).

| PDE | Parameter | Metric | Baseline model | |
|---------------------------------------|---|----------------------|----------------------|----------------------|
| | | | U-Net | FNO |
| 2DCFD | $M = 0.1$, inviscid Rand periodic | RMSE | 4.0×10^{-1} | 2.6×10^{-1} |
| | | nRMSE | 6.6×10^{-1} | 2.8×10^{-1} |
| | | max error | $5.1 \times 10^{+0}$ | $4.2 \times 10^{+0}$ |
| | | cRMSE | 1.5×10^{-1} | 1.6×10^{-2} |
| | | bRMSE | 4.3×10^{-1} | 2.6×10^{-1} |
| | | fRMSE low | 1.1×10^{-1} | 4.5×10^{-2} |
| | | fRMSE mid | 4.8×10^{-2} | 4.4×10^{-2} |
| | | fRMSE high | 1.7×10^{-2} | 1.6×10^{-2} |
| | $M = 0.1, \eta = \zeta = 0.01$ Rand periodic | RMSE | 9.1×10^{-2} | 2.3×10^{-2} |
| | | nRMSE | 7.1×10^{-1} | 1.7×10^{-1} |
| | | max error | $1.1 \times 10^{+0}$ | 4.0×10^{-1} |
| | | cRMSE | 3.6×10^{-2} | 5.3×10^{-3} |
| | | bRMSE | 1.1×10^{-1} | 2.2×10^{-2} |
| | | fRMSE low | 2.7×10^{-2} | 5.7×10^{-3} |
| | | fRMSE mid | 8.2×10^{-3} | 2.7×10^{-3} |
| | | fRMSE high | 2.6×10^{-3} | 6.3×10^{-4} |
| | $M = 0.1, \eta = \zeta = 0.1$ Rand periodic | RMSE | 4.7×10^{-2} | 4.9×10^{-3} |
| | | nRMSE | $5.1 \times 10^{+0}$ | 3.6×10^{-1} |
| | | max error | 6.7×10^{-1} | 8.7×10^{-2} |
| | | cRMSE | 3.2×10^{-2} | 3.2×10^{-3} |
| | | bRMSE | 6.6×10^{-2} | 4.3×10^{-3} |
| | | fRMSE low | 1.3×10^{-2} | 1.4×10^{-3} |
| | | fRMSE mid | 4.2×10^{-3} | 4.3×10^{-4} |
| | | fRMSE high | 2.2×10^{-3} | 1.4×10^{-4} |
| $M = 1.0$, inviscid Rand periodic | RMSE | $1.5 \times 10^{+0}$ | $1.4 \times 10^{+0}$ | |
| | nRMSE | 4.7×10^{-1} | 3.5×10^{-1} | |
| | max error | $1.6 \times 10^{+1}$ | $1.6 \times 10^{+1}$ | |
| | cRMSE | 4.8×10^{-1} | 1.6×10^{-1} | |
| | bRMSE | $1.5 \times 10^{+0}$ | $1.3 \times 10^{+0}$ | |
| | fRMSE low | 4.8×10^{-1} | 4.0×10^{-1} | |
| | fRMSE mid | 1.2×10^{-1} | 1.2×10^{-1} | |
| | fRMSE high | 3.9×10^{-2} | 3.9×10^{-2} | |

Table 12: Summary of the baseline models' performance for different evaluation metrics: RMSE, normalised RMSE (nRMSE), RMSE from conserved value (cRMSE), maximum error, RMSE at the boundaries (bRMSE), RMSE in Fourier space at low (fRMSE low), medium (fRMSE mid), and high frequency (fRMSE high) ranges applied to the 2d compressible Navier-Stokes equation with different parameter values (second part).

| PDE | Parameter | Metric | Baseline model | |
|------------|---|----------------------|----------------------|----------------------|
| | | | U-Net | FNO |
| 2DCFD | $M = 1.0, \eta = \zeta = 0.01$ Rand periodic | RMSE | 3.4×10^{-1} | 1.2×10^{-1} |
| | | nRMSE | 3.6×10^{-1} | 9.6×10^{-2} |
| | | max error | $3.7 \times 10^{+0}$ | $1.7 \times 10^{+0}$ |
| | | cRMSE | 1.1×10^{-1} | 1.8×10^{-2} |
| | | bRMSE | 3.6×10^{-1} | 1.3×10^{-1} |
| | | fRMSE low | 1.1×10^{-1} | 3.3×10^{-2} |
| | | fRMSE mid | 2.7×10^{-2} | 1.5×10^{-2} |
| | | fRMSE high | 6.2×10^{-3} | 3.6×10^{-3} |
| | $M = 1.0, \eta = \zeta = 0.1$ Rand periodic | RMSE | 1.1×10^{-1} | 1.5×10^{-2} |
| | | nRMSE | 9.2×10^{-1} | 9.8×10^{-2} |
| | | max error | $1.3 \times 10^{+0}$ | 2.4×10^{-1} |
| | | cRMSE | 4.8×10^{-2} | 4.8×10^{-3} |
| | | bRMSE | 1.5×10^{-1} | 1.7×10^{-2} |
| | | fRMSE low | 3.0×10^{-2} | 3.2×10^{-3} |
| | | fRMSE mid | 1.3×10^{-2} | 1.5×10^{-3} |
| | | fRMSE high | 4.3×10^{-3} | 8.9×10^{-4} |
| | $M = 0.1$, inviscid Turb periodic | RMSE | 3.3×10^{-1} | 2.8×10^{-1} |
| | | nRMSE | 1.9×10^{-1} | 1.6×10^{-1} |
| | | max error | $2.2 \times 10^{+0}$ | $1.8 \times 10^{+0}$ |
| | | cRMSE | 1.5×10^{-2} | 1.2×10^{-2} |
| | | bRMSE | 3.6×10^{-1} | 2.8×10^{-1} |
| | | fRMSE low | 6.5×10^{-2} | 5.0×10^{-2} |
| | | fRMSE mid | 3.2×10^{-2} | 3.1×10^{-2} |
| | | fRMSE high | 8.5×10^{-3} | 6.5×10^{-3} |
| | $M = 1.0$, inviscid Turb periodic | RMSE | 9.5×10^{-2} | 9.2×10^{-2} |
| | | nRMSE | 1.4×10^{-1} | 1.3×10^{-1} |
| | | max error | 8.2×10^{-1} | 7.9×10^{-1} |
| | | cRMSE | 6.5×10^{-3} | 4.3×10^{-3} |
| bRMSE | | 1.1×10^{-1} | 9.7×10^{-1} | |
| fRMSE low | | 1.3×10^{-2} | 1.1×10^{-2} | |
| fRMSE mid | | 1.2×10^{-2} | 1.2×10^{-2} | |
| fRMSE high | | 5.2×10^{-3} | 5.2×10^{-3} | |

Table 13: Summary of the baseline models’ performance for different evaluation metrics: RMSE, normalised RMSE (nRMSE), RMSE from conserved value (cRMSE), maximum error, RMSE at the boundaries (bRMSE), RMSE in Fourier space at low (fRMSE low), medium (fRMSE mid), and high frequency (fRMSE high) ranges applied to the 3d compressible Navier-Stokes equation with different parameter values.

| PDE | Parameter | Metric | Baseline model | |
|------------|-------------------------------------|----------------------|----------------------|----------------------|
| | | | U-Net | FNO |
| 3DCFD | $M = 1.0$ inviscid Rand periodic | RMSE | $2.2 \times 10^{+0}$ | 6.0×10^{-1} |
| | | nRMSE | $1.0 \times 10^{+0}$ | 3.7×10^{-1} |
| | | max error | $9.0 \times 10^{+0}$ | $3.6 \times 10^{+0}$ |
| | | cRMSE | $2.3 \times 10^{+0}$ | 8.1×10^{-2} |
| | | bRMSE | $2.1 \times 10^{+0}$ | 6.0×10^{-1} |
| | | fRMSE low | 7.3×10^{-1} | 1.1×10^{-1} |
| | | fRMSE mid | 7.6×10^{-2} | 4.4×10^{-2} |
| | | fRMSE high | 2.3×10^{-2} | 9.3×10^{-3} |
| | $M = 1.0$ inviscid Turb periodic | RMSE | 8.1×10^{-2} | 8.2×10^{-2} |
| | | nRMSE | 2.3×10^{-1} | 2.4×10^{-1} |
| | | max error | 5.0×10^{-1} | 4.5×10^{-1} |
| | | cRMSE | 7.3×10^{-3} | 2.8×10^{-3} |
| | | bRMSE | 9.9×10^{-2} | 8.6×10^{-2} |
| | | fRMSE low | 1.1×10^{-2} | 7.2×10^{-3} |
| fRMSE mid | 8.0×10^{-3} | 9.4×10^{-3} | | |
| fRMSE high | 1.7×10^{-3} | 4.5×10^{-3} | | |

F Detailed Runtime Comparison

In this section we present the detailed comparison of computation time between the PDE solver used to generate the data and the baseline models used in this work, summarized in Table 15. The system listed in Table 14 was used to run all timing measurements regarding the Diffusion-sorption, 2D diffusion-reaction and Shallow-water equation scenarios. PyClaw [23], a well-optimized finite-volume Fortran code, is used as PDE solver for the shallow-water equation data generation. Note that the experiment is only running on a single core due to its small size. Because the PINN model is not discretized, the inference time includes evaluating the trained model at the same discretization points of the reference simulation for the last 20 time steps of the data. E.g. the 2D diffusion-reaction scenario is evaluated at $128^2 \times 20$ discrete points. Additionally, autoregression is not required and therefore, it leads to significantly faster computation time relative to FNO and U-Net.

Table 14: System configuration 1

| | |
|----------|------------------------------|
| CPU | $2 \times$ AMD EPYC 7742 |
| GPU | $1 \times$ NVIDIA Volta V100 |
| Software | PyTorch@1.11, CUDA@11.3 |

Table 15: Comparison of computation time between the PDE solver used to generate a single data sample and single forward runs of FNO, U-Net, and PINN. Training time of the baseline models for one epoch are also presented in this table. The unit used for the time is seconds.

| PDE | Resolution | Model | Training time ($\frac{s}{epoch}$) | Epochs | Inference time (s) |
|------------------------|------------|------------|-------------------------------------|--------|--------------------|
| Diffusion-sorption | 1024^1 | PDE solver | – | – | 59.83 |
| | | FNO | 97.52 | 500 | 0.32 |
| | | U-Net | 96.75 | 500 | 0.32 |
| | | PINN | 0.011 | 15 000 | 0.0027 |
| 2D diffusion-reaction | 128^2 | PDE solver | – | – | 2.21 |
| | | FNO | 108.28 | 500 | 0.40 |
| | | U-Net | 83.19 | 500 | 0.61 |
| | | PINN | 0.022 | 100 | 0.0077 |
| Shallow-water equation | 128^2 | PDE solver | – | – | 0.62 |
| | | FNO | 105.16 | 500 | 0.37 |
| | | U-Net | 83.32 | 500 | 0.56 |
| | | PINN | 0.041 | 15 000 | 0.00673 |

As the case for 3D data, we also performed a similar experiment whose results are summarized in Table 17. The used system information is listed in Table 16. Because of the severe memory usage, the resolution was reduced to 64^3 , though we provided a data with resolution 128^3 in our official dataset. Note that the training and inference time are shorter than the 2D cases in Table 15. This is because the number of time-step and sample numbers are less than the 2D cases to reduce dataset size.

Table 16: System configuration 2

| | |
|------------------------|------------------------------------|
| GPU | $1 \times$ NVIDIA GeForce RTX 3090 |
| Software (ML methods) | PyTorch@1.11, CUDA@11.3 |
| Software (simulations) | JAX@0.2.26, CUDA@11.3 |

G Resolution Sensitivity of Inference Time

Figure 13 plots the resolution dependence of the inference time of classical simulation and ML methods for 2D/3D compressible Navier-Stokes equations cases. To calculate the inference times, we used the same hardware resources to be a "fair" comparison as listed in Table 16.

Table 17: Comparison of computation time between the PDE solver used to generate a single data sample and single forward runs of FNO, U-Net. Training time of the baseline models for one epoch are also presented in this table. The unit used for the time is seconds.

| PDE | Resolution | Model | Training time ($\frac{s}{epoch}$) | Epochs | Inference time (s) |
|--------|------------|------------|-------------------------------------|--------|--------------------|
| 3D CFD | 64^3 | PDE solver | – | – | 60.07 |
| | | FNO | 24.77 | 500 | 0.14 |
| | | U-Net | 62.22 | 500 | 0.27 |

The figure clearly shows that the ML inference time is nearly 3-order of magnitude smaller than that of the classical simulations. Concerning the resolution dependence, both of the ML models show a similar dependence to the inviscid classical simulation method. Importantly, the inference time of ML models is in general independent of the diffusion coefficient, such as viscosity. On the other hand, the classical simulation methods increase their computation time with diffusion coefficient because of the stability condition, known as Courant-Friedrich-Lewy (CFL) condition, $\Delta t \propto \Delta x^2/\eta$ in the case of the explicit method. Here Δx , Δt are time-step size and mesh size, respectively, and η is the diffusion coefficient. This is much severer restriction than the inviscid case whose CFL condition is $\Delta t \propto \Delta x$. Hence, we can conclude that ML methods could even be suitable for solving for the problem with including strong-diffusive regime.

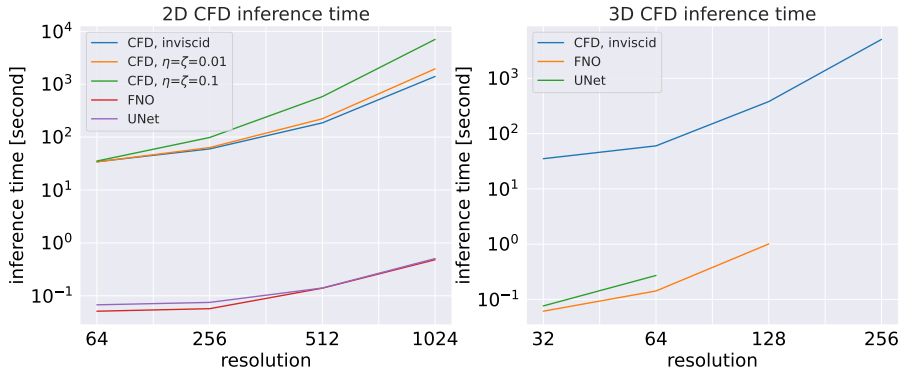


Figure 13: Plots inference time for 2D/3D CFD cases.

H Error Comparison with PDE Solver

To further assess the benefit of the trained baseline models, we generated the 2D diffusion-reaction data using a PDE solver with higher resolution (512×512), and downsampled them to lower resolution (128×128). These downsampled data were assumed as the ground truth (low discretization error) and then were used to train the baseline models. The trained baseline model predictions were compared against data that were generated using the same PDE solver but with coarser resolution (higher discretization error). The error comparison is summarized in Table 18. We observed that generating the data with lower resolution already accumulates high discretization error, relative to the baseline model prediction error. However, further sensitivity analysis with regards to different resolutions is required in future works to determine if the resolution is fine enough to be assumed as the ground truth.

I Visualization of Model Predictions

In this section, we present visualizations of the baseline model predictions, compared against the generated datasets for the diffusion-sorption equation (Figure 14), 2D diffusion-reaction equation (Figure 15, Figure 16, and Figure 17), the shallow-water equation (Figure 18, Figure 19, and Figure 20), 1D Advection equation Figure 21, 1D Burgers equation Figure 22, 1D Reaction-Diffusion

Table 18: Error comparison between of U-Net, FNO, and PINN prediction, as well as low-resolution PDE solver data, against the high-resolution PDE solver data (assumed as the ground truth) for the 2D diffusion-reaction scenario.

| Error metric | U-Net | FNO | PINN | low-res PDE solver |
|--------------|----------------------|----------------------|----------------------|----------------------|
| RMSE | 6.1×10^{-2} | 8.1×10^{-3} | 1.9×10^{-1} | 1.8×10^{-1} |
| nRMSE | 8.4×10^{-1} | 1.2×10^{-1} | $1.6 \times 10^{+0}$ | $2.8 \times 10^{+0}$ |
| max error | 1.9×10^{-1} | 9.1×10^{-2} | 5.0×10^{-1} | 8.9×10^{-1} |
| cRMSE | 3.9×10^{-2} | 1.7×10^{-3} | 1.3×10^{-1} | 4.9×10^{-2} |
| bRMSE | 7.8×10^{-2} | 2.7×10^{-2} | 2.2×10^{-1} | 2.1×10^{-1} |
| fRMSE low | 1.7×10^{-2} | 8.2×10^{-4} | 5.7×10^{-2} | 4.9×10^{-2} |
| fRMSE mid | 5.4×10^{-3} | 7.7×10^{-4} | 1.3×10^{-2} | 2.2×10^{-2} |
| fRMSE high | 6.8×10^{-4} | 4.1×10^{-4} | 1.5×10^{-3} | 3.4×10^{-3} |

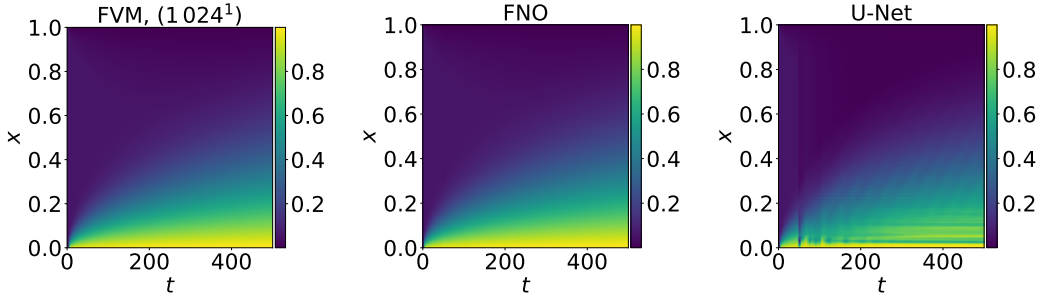


Figure 14: Visualization of the diffusion-sorption equation (a) data, (b) FNO prediction, and (c) U-Net prediction.

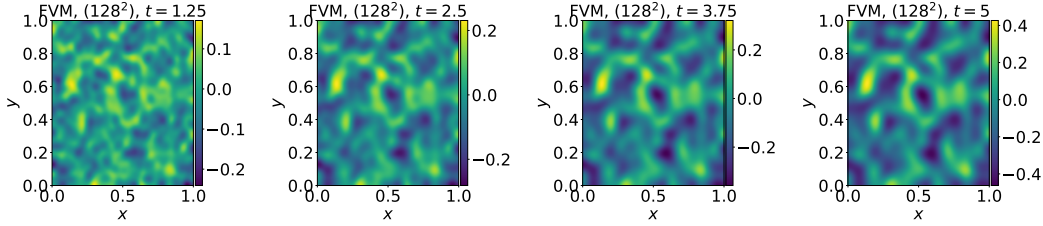


Figure 15: Visualization of the time evolution of the 2D diffusion-reaction equation data.

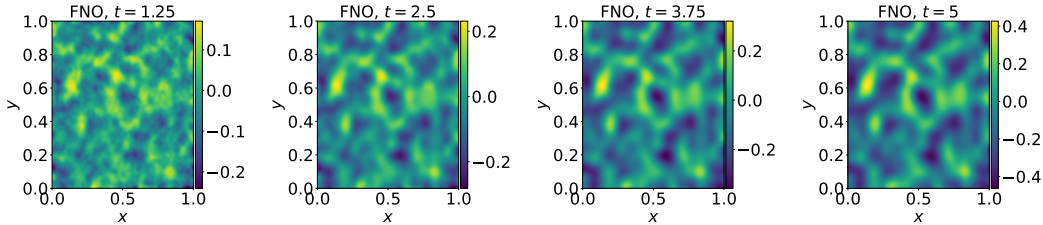


Figure 16: Visualization of the time evolution of the 2D diffusion-reaction equation predicted using FNO.

equation Figure 23, 1D compressible NS equations Figure 24, 2D Darcy flow Figure 25, and 2D compressible NS equations Figure 26.

J Visualization of Initial Conditions

In this section, we provide a collection of initial condition visualizations for each problem. Figure 27 shows different radius of the initial perturbation used as the initial condition for five different samples

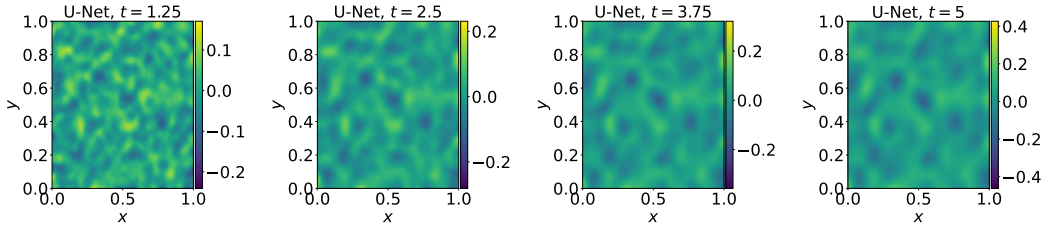


Figure 17: Visualization of the time evolution of the 2D diffusion-reaction equation predicted using U-Net.

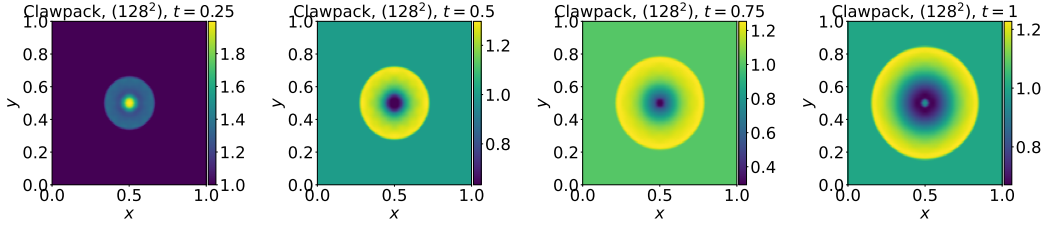


Figure 18: Visualization of the time evolution of the shallow water equation data.

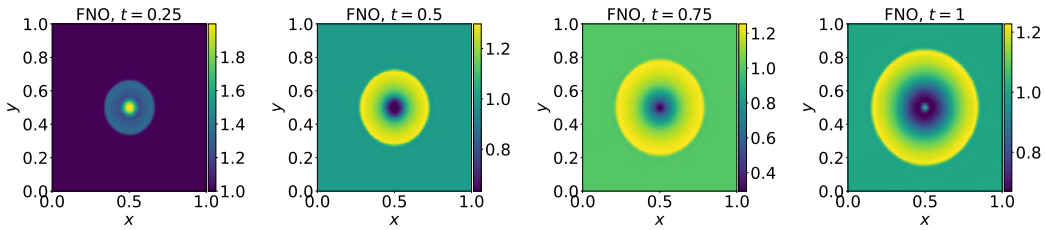


Figure 19: Visualization of the time evolution of the shallow water equation predicted using FNO.

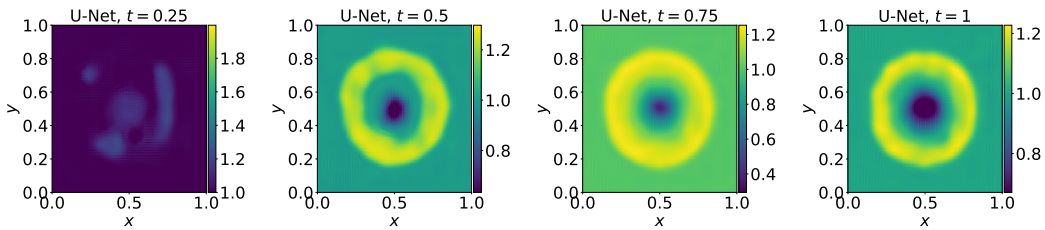


Figure 20: Visualization of the time evolution of the shallow water equation predicted using U-Net.

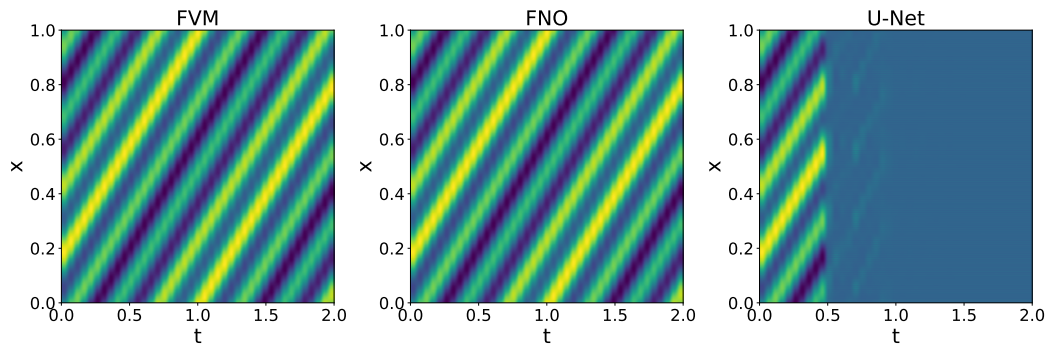


Figure 21: Plots of the predictions for 1D Advection equation.

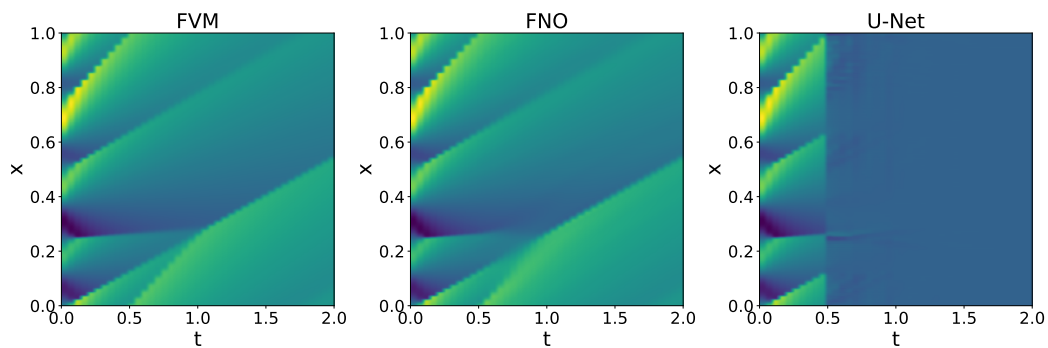


Figure 22: Plots of the predictions for 1D Burgers equation.

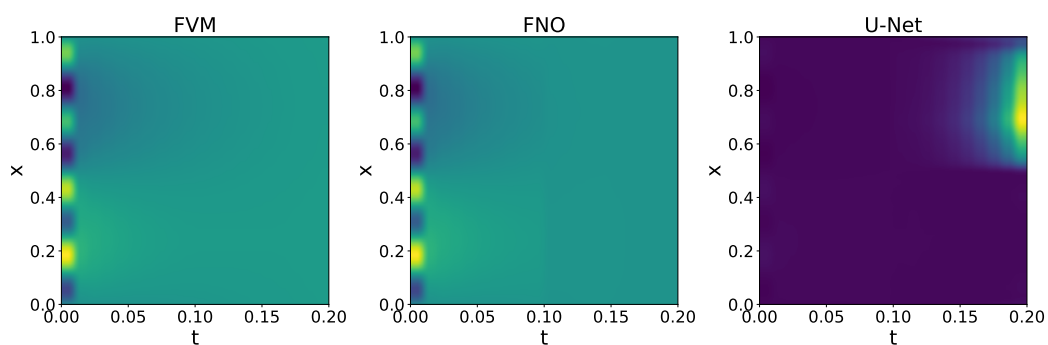


Figure 23: Plots of the predictions for 1D Reaction-Diffusion equation.

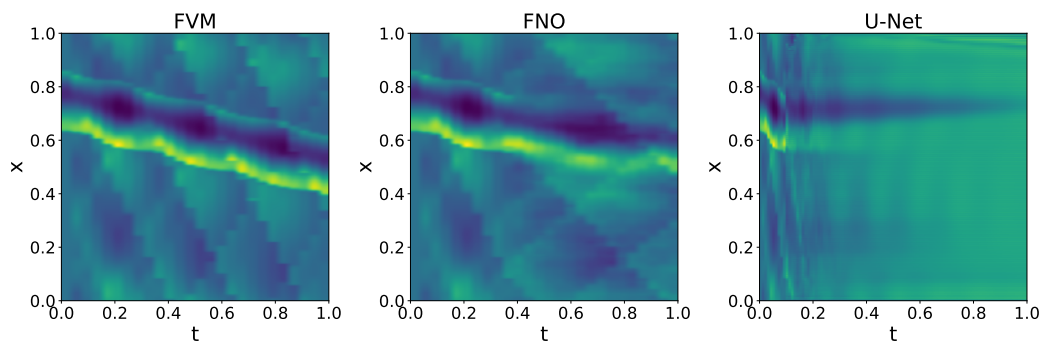


Figure 24: Plots of the predictions of density for 1D compressible NS equations.

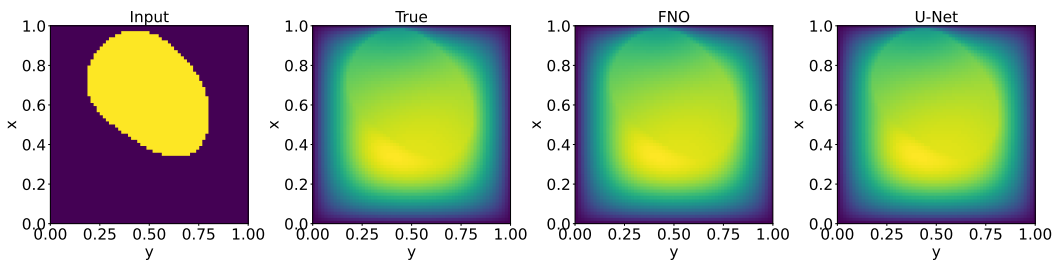


Figure 25: Plots of the predictions for 2D Darcy Flow.

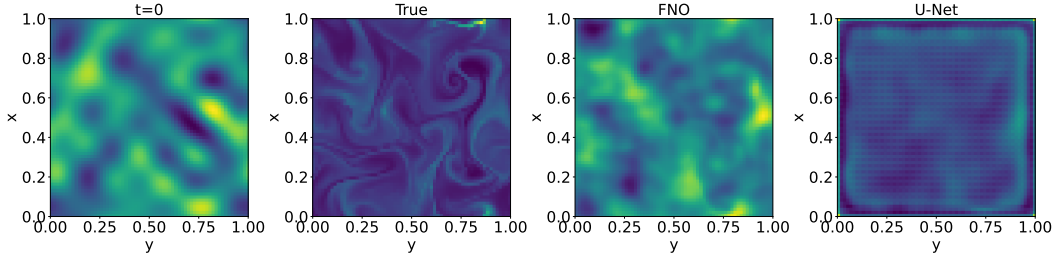


Figure 26: Plots of the predictions of the density for 2D compressible NS equations at the final time-step.

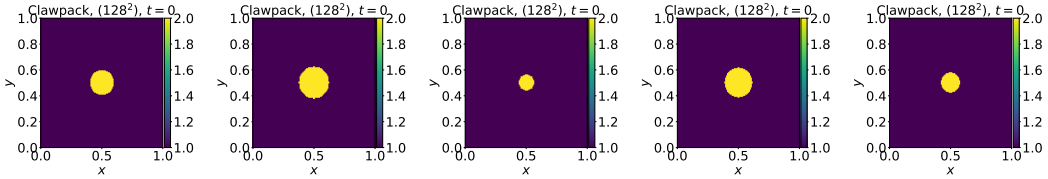


Figure 27: Visualization of the different radius of the initial perturbation used for the 2D shallow-water equations data.

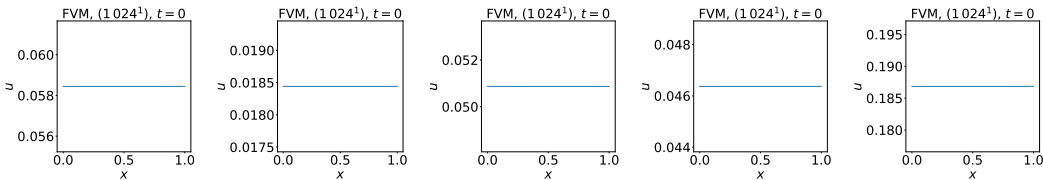


Figure 28: Visualization of the random uniform initial conditions used for the 1D diffusion-sorption equations data.

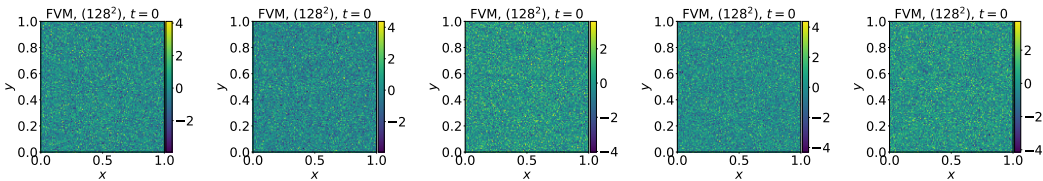


Figure 29: Visualization of the random initial conditions used for the 2D diffusion-reaction equations data.

of the 2D shallow-water equation data. Figure 28 shows different random uniform initial condition used for five different samples of the 1D diffusion-sorption equation data. Figure 29 shows different random noise used as the initial condition for five different samples of the 2D diffusion-reaction equation data.

In Figure 30, we plotted the several samples of the initial condition for 1D Advection and Burgers equations. Figure 31 is also the similar plot of the initial condition for 1D Diffusion-Reaction equation. Note that in this case the value of the scalar function is limited between 0 to 1 because of the form of the source term. Finally, we provided several samples of the 1D and 2D CFD cases in Figure 32 and Figure 33.

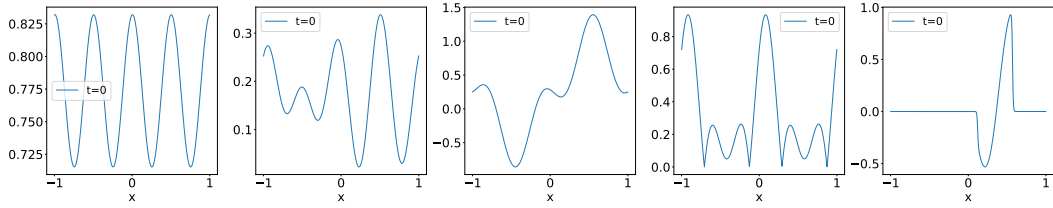


Figure 30: Visualization of the random initial conditions used for the 1D Advection/Burgers equations data.

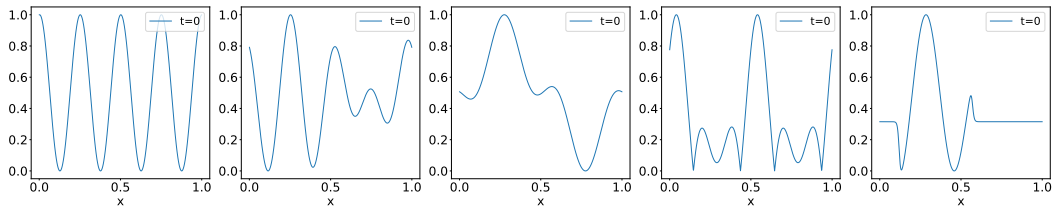


Figure 31: Visualization of the random initial conditions used for the 1D Reaction-Diffusion equations data.

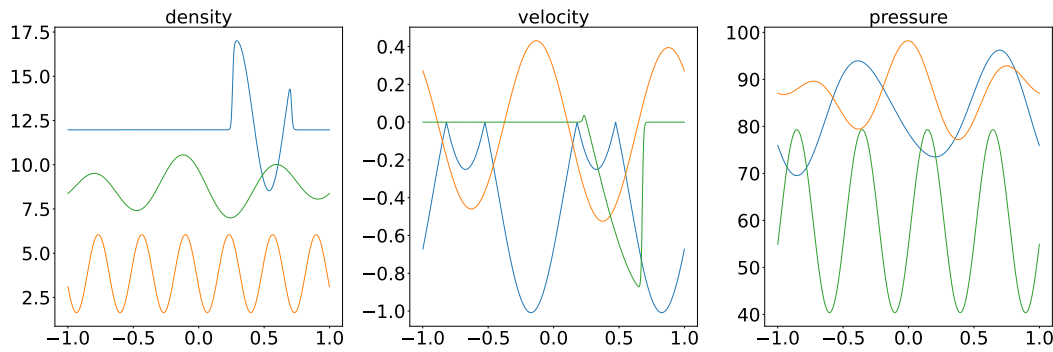


Figure 32: Visualization of the random initial conditions used for the 1D CFD data. The different colors mean the different samples.

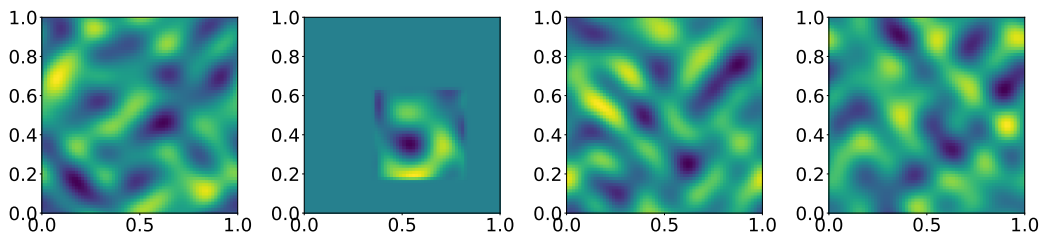


Figure 33: Visualization of the initial conditions of density used for the 2D CFD data.

K PDEBENCH’s Data Sheet

In this section, we provide more detailed information about the DaRUS Dataverse which PDEBENCH uses to store its datasets. As explained in subsection 3.5, DaRUS is the University of Stuttgart’s data repository based on the OpenSource Software DataVerse3, providing a place to archive, share, and publish the research data, scripts and source codes. All data uploaded to DaRUS gets a DOI as a persistent identifier, a license, and can be described with an extensive set of metadata, organized in metadata blocks. A dedicated team ensures that DaRUS is continuously maintained. PDEBENCH obtained a permanent DOI (doi:10.18419/darus-2986) [55] through DaRUS.

K.1 Motivation

1. **For what purpose was the dataset created?** *Was there a specific task in mind? Was there a specific gap that needed to be filled? Please provide a description.*

PDEBENCH’s datasets were created to provide a more challenging and representative benchmark for scientific ML approaches, that is, machine learning methods to approximately simulate physical systems governed by PDEs. More details can be found in section 1.

2. **Who created this dataset (e.g. which team, research group) and on behalf of which entity (e.g., company, institution, organization)?**

This dataset was created by Makoto Takamoto and Francesco Alesiani (senior researchers at NEC Labs Europe), Dan MacKinlay (postdoctoral researcher at CSIRO’s Data61), Timothy Praditia and Raphael Leiteritz (PhD students at the University of Stuttgart), Dirk Pflüger and Mathias Niepert (professors at the University of Stuttgart).

3. **Who funded the creation of the dataset?** *If there is an associated grant, please provide the name of the grantor and the grant name and number.*

Funding for the University of Stuttgart researchers was provided by the Deutsche Forschungsgemeinschaft (DFG, German Research Foundation) under Germany’s Excellence Strategy - EXC 2075 – 390740016, for the Cluster of Excellence on “Data-Integrated Simulation Science (SimTech)”.

4. **Any other comments?**

No

K.2 Composition

1. **What do the instances that comprise the dataset represent (e.g. documents, photos, people, countries)?** *Are there multiple types of instances (e.g. movies, users, and ratings; people and interactions between them; nodes and edges)? Please provide a description.*

Each instance of the dataset is a simulation-generated array, containing the solutions (i.e. values of the variables of interest) of a specific partial differential equation (PDE). The details of the physical systems governed by PDEs can be found in Appendix D and the format of the data can be found in subsection K.10.

2. **How many instances are there in total (of each type, if appropriate)?** An overview of the datasets and instances are provided in Table 1. For the 1D diffusion-sorption equation, there is one file containing 10 000 samples, with 1 024 spatial cells, 101 time steps, and 1 variable. For the 2D diffusion-reaction equation, there is one file containing 1 000 samples, with 128×128 spatial cells, 101 time steps, and 2 variables. For the 2D shallow-water equation, there is one file containing 1 000 samples, with 128×128 spatial cells, 101 time steps, and 1 variable. For the advection, Burgers, and 1D-diffusion-reaction equation, each file contains 10 000 samples, with 1 024 spatial cells, 201 time steps, and 1 variable. The advection equation has 6 files for different parameters (advection velocity), the Burgers equation has 12 files for different parameters (diffusion coefficient), and the 1D diffusion-reaction equation has 16 files for different parameters (diffusion and source term coefficients). For the DarcyFlow, each file contains 10 000 samples, with 128×128 spatial cells, 1 time step, and 2 variables. For the incompressible Navier-Stokes equations, the file contains 1 000 samples, with 256×256 spatial cells, 1 000 time steps, and 2 variables. For the 1D compressible Navier-Stokes equations, the file contains 10 000 samples, with 1 024 spatial cells, 100 time steps, and 3 variables. For the 2D compressible Navier-Stokes equations,

the file contains 1 000 samples, with 512×512 spatial cells, 21 time steps, and 4 variables. For the 3D compressible Navier-Stokes equations, the file contains 1 00 samples, with $128 \times 128 \times 128$ spatial cells, 21 time steps, and 5 variables. The variation of parameters, initial conditions, and boundary conditions of the compressible Navier-Stokes equations are provided in subsection D.5.

3. **Does the dataset contain all possible instances or is it a sample (not necessarily random) of instances from a larger set?** *If the dataset is a sample, then what is the larger set? Is the sample representative of the larger set (e.g. geographic coverage)? If so, please describe how this representativeness was validated/verified. If it is not representative of the larger set, please describe why not (e.g., to cover a more diverse range of instances, because instances were withheld or unavailable.)*

The datasets that we provide are intended to be representative of challenging physical systems. Since this is a very broad and general scope, it is difficult, if not impossible, to represent it wholly. However, we provide datasets that contain longer time steps, non-linearly coupled variables, various challenging boundary conditions, different parameters, and more applicable to real-world scenarios than currently available. For more details, see subsection 3.2 and Appendix D.

4. **What data does each instance consist of?** *("Raw" data (e.g. unprocessed text or images) or features? In either case, please provide a description.)*

Each instance consists of numerical values in the form of an HDF5 file that correspond to the variables of interest in each specific physical system. See Appendix D for further details.

5. **Is there a label or target associated with each instance? If so, please provide a description.**

Each instance is an array, which elements are the values of a specific variable at a specific space and time (for the data format please refer to subsection K.10). These values are the target for the regression task performed by the baseline models. We also provide the full information of physical parameters for each dataset.

6. **Is any information missing from individual instances?** *(If so, please provide a description, explaining why this information is missing (e.g., because it was unavailable). This does not include intentionally removed information, but might include, e.g., redacted text.)*

No.

7. **Are relationships between individual instances made explicit (e.g., users' movie ratings, social network links)?** *(If so, please describe how these relationships are made explicit.)*

There are no relationships between different instances which were generated using randomly created initial conditions.

8. **Are there recommended data splits (e.g., training, development/validation, testing)?** *(If so, please provide a description of these splits, explaining the rationale behind them.)*

There are no recommendations for the data split. Users can experiment defining the data split as a hyperparameter. However, for the paper we use the split of 90% for training and the rest for validation and testing.

9. **Are there any errors, sources of noise, or redundancies in the dataset?** *(If so, please provide a description.)*

No. The only possible source of error might come from the discretization error, which should be minimal because our dataset was generated with a relatively high resolution. However, users can also generate their own dataset with the provided source code with even higher resolution.

10. **Is the dataset self-contained, or does it link to or otherwise rely on external resources (e.g., websites, tweets, other datasets)?** *(If it links to or relies on external resources, a) are there guarantees that they will exist, and remain constant, over time; b) are there official archival versions of the complete dataset (i.e., including the external resources as they existed at the time the dataset was created); c) are there any restrictions (e.g., licenses, fees) associated with any of the external resources that might apply to a future user? Please provide descriptions of all external resources and any restrictions associated with them, as well as links or other access points, as appropriate.)*

The dataset is available via a data repository (DaRUS) [10], which is maintained by the University of Stuttgart, and therefore will be available permanently.

11. **Does the dataset contain data that might be considered confidential (e.g., data that is protected by legal privilege or by doctor-patient confidentiality, data that includes the content of individuals' non-public communications)?** *(If so, please provide a description.)*
No.
12. **Does the dataset contain data that, if viewed directly, might be offensive, insulting, threatening, or might otherwise cause anxiety?** *(If so, please describe why.)*
No.
13. **Does the dataset relate to people?** *(If not, you may skip the remaining questions in this section.)*
No.
14. **Does the dataset identify any subpopulations (e.g., by age, gender)?** *(If so, please describe how these subpopulations are identified and provide a description of their respective distributions within the dataset.)*
N/A.
15. **Is it possible to identify individuals (i.e., one or more natural persons), either directly or indirectly (i.e., in combination with other data) from the dataset?** *(If so, please describe how.)*
N/A.
16. **Does the dataset contain data that might be considered sensitive in any way (e.g., data that reveals racial or ethnic origins, sexual orientations, religious beliefs, political opinions or union memberships, or locations; financial or health data; biometric or genetic data; forms of government identification, such as social security numbers; criminal history)?** *(If so, please provide a description.)*
N/A.
17. **Any other comments?**
No.

K.3 Collection Process

1. **How was the data associated with each instance acquired?** (Was the data directly observable (e.g., raw text, movie ratings), reported by subjects (e.g., survey responses), or indirectly inferred/derived from other data (e.g., part-of-speech tags, model-based guesses for age or language)? If data was reported by subjects or indirectly inferred/derived from other data, was the data validated/verified? If so, please describe how.)
All the dataset were obtained by performing computationally expensive numerical simulations for each PDEs.
2. **What mechanisms or procedures were used to collect the data (e.g., hardware apparatus or sensor, manual human curation, software program, software API)?** (How were these mechanisms or procedures validated?)
The numerical simulations were performed either using CPUs or GPUs with freely available Python libraries, such as Scipy.
3. **If the dataset is a sample from a larger set, what was the sampling strategy (e.g., deterministic, probabilistic with specific sampling probabilities)?**
This is already mentioned above (F.2 "Composition"'s 3rd item).
4. **Who was involved in the data collection process (e.g., students, crowdworkers, contractors) and how were they compensated (e.g., how much were crowdworkers paid)?**
All the data generation process (numerical simulation) was performed by the authors, mainly conducted by Makoto Takamoto, Timothy Praditia, Raphael Leiteritz, Dan MacKinlay and Francesco Alesiani. For a part of the simulations we received help by people at ANU Techlauncher who are acknowledged in "Acknowledgements".
5. **Over what timeframe was the data collected?** (Does this timeframe match the creation timeframe of the data associated with the instances (e.g., recent crawl of old news articles)? If not, please describe the timeframe in which the data associated with the instances was created.)

The dataset was generated from early to mid 2022. Because of the eternal nature of PDEs, our dataset is irrelevant to the timeframe of creation.

6. **Were any ethical review processes conducted (e.g., by an institutional review board)?** (If so, please provide a description of these review processes, including the outcomes, as well as a link or other access point to any supporting documentation.)
No.
7. **Does the dataset relate to people?** (If not, you may skip the remaining questions in this section.)
No
8. **Did you collect the data from the individuals in question directly, or obtain it via third parties or other sources (e.g., websites)?**
No.
9. **Were the individuals in question notified about the data collection?** (If so, please describe (or show with screenshots or other information) how notice was provided, and provide a link or other access point to, or otherwise reproduce, the exact language of the notification itself.)
N/A.
10. **Did the individuals in question consent to the collection and use of their data?** (If so, please describe (or show with screenshots or other information) how consent was requested and provided, and provide a link or other access point to, or otherwise reproduce, the exact language to which the individuals consented.)
N/A.
11. **If consent was obtained, were the consenting individuals provided with a mechanism to revoke their consent in the future or for certain uses?** (If so, please provide a description, as well as a link or other access point to the mechanism (if appropriate).)
N/A.
12. **Has an analysis of the potential impact of the dataset and its use on data subjects (e.g., a data protection impact analysis) been conducted?** (If so, please provide a description of this analysis, including the outcomes, as well as a link or other access point to any supporting documentation.)
N/A.
13. Any other comments?
None.

K.4 Preprocessing/cleaning/labeling

1. **Was any preprocessing/cleaning/labeling of the data done (e.g., discretization or bucketing, tokenization, part-of-speech tagging, SIFT feature extraction, removal of instances, processing of missing values)?** (If so, please provide a description. If not, you may skip the remainder of the questions in this section.)
No. At most we rejected meaningless solutions because of the failure of numerical simulations, such as data with all zeros or Nan values.
2. **Was the "raw" data saved in addition to the preprocessed/cleaned/labeled data (e.g., to support unanticipated future uses)?** (If so, please provide a link or other access point to the "raw" data.)
N/A.
3. **Is the software used to preprocess/clean/label the instances available?** (If so, please provide a link or other access point.)
N/A.
4. **Any other comments?**
None.

K.5 Uses

1. **Has the dataset been used for any tasks already?** (If so, please provide a description.)
Not yet.
2. **Is there a repository that links to any or all papers or systems that use the dataset?** (If so, please provide a link or other access point.)
No.
3. **What (other) tasks could the dataset be used for?**
The dataset could possibly be used for developing or testing ML models for fitting the out-of-distribution data, such as unseen physical parameters.
4. **Is there anything about the composition of the dataset or the way it was collected and preprocessed/cleaned/labeled that might impact future uses?** (For example, is there anything that a future user might need to know to avoid uses that could result in unfair treatment of individuals or groups (e.g., stereotyping, quality of service issues) or other undesirable harms (e.g., financial harms, legal risks) If so, please provide a description. Is there anything a future user could do to mitigate these undesirable harms?)
Basically no. But high-dimensional data, in particular 3D data, has a relatively small number of samples, only 100, due of storage limitations and the very large size of single data points. This might result in ML models with insufficient accuracy, but it is realistic for scientific simulations, where extensive computation time can be required for a single data point. However, we emphasize that we provide the data generation source code. This allows future users to increase their dataset size as much as they need.
5. **Are there tasks for which the dataset should not be used?** (If so, please provide a description.)
No.
6. **Any other comments?**
None.

K.6 Distribution

1. **Will the dataset be distributed to third parties outside of the entity (e.g., company, institution, organization) on behalf of which the dataset was created?** (If so, please provide a description.)
Yes, the dataset is freely and publicly available and accessible.
2. **How will the dataset will be distributed (e.g., tarball on website, API, GitHub)?** (Does the dataset have a digital object identifier (DOI)?)
The dataset is free for download either by directly accessing the DaRUS page <https://doi.org/10.18419/darus-2986> or making use of a Python API, "pyDaRUS", provided by DaRUS. An example of a code snippet for downloading the data is listed in subsection 3.5.
3. **When will the dataset be distributed?**
The dataset is distributed as of June 2022 in its first version.
4. **Will the dataset be distributed under a copyright or other intellectual property (IP) license, and/or under applicable terms of use (ToU)?** (If so, please describe this license and/or ToU, and provide a link or other access point to, or otherwise reproduce, any relevant licensing terms or ToU, as well as any fees associated with these restrictions.)
The dataset is licensed under CC BY license.
5. **Have any third parties imposed IP-based or other restrictions on the data associated with the instances?** (If so, please describe these restrictions, and provide a link or other access point to, or otherwise reproduce, any relevant licensing terms, as well as any fees associated with these restrictions.)
No
6. **Do any export controls or other regulatory restrictions apply to the dataset or to individual instances?** (If so, please describe these restrictions, and provide a link or other access point to, or otherwise reproduce, any supporting documentation.)
No

7. Any other comments?

None.

K.7 Maintenance

1. Who is supporting/hosting/maintaining the dataset?

The storage infrastructure, DaRUS, is maintained by the University of Stuttgart and a dedicated team of DaRUS. The dataset themselves are maintained by the authors.

2. How can the owner/curator/manager of the dataset be contacted (e.g., email address)?

E-mail addresses are provided in the main-body of the paper.

3. Is there an erratum? (If so, please provide a link or other access point.)

Currently, no. As errors are encountered, future versions of the dataset may be released. They will all be provided in the same github and DaRUS location.

4. Will the dataset be updated (e.g., to correct labeling errors, add new instances, delete instances)? (If so, please describe how often, by whom, and how updates will be communicated to users (e.g., mailing list, GitHub)?)

Same as previous.

5. If the dataset relates to people, are there applicable limits on the retention of the data associated with the instances (e.g., were individuals in question told that their data would be retained for a fixed period of time and then deleted)? (If so, please describe these limits and explain how they will be enforced.)

N/A.

6. Will older versions of the dataset continue to be supported/hosted/maintained? (If so, please describe how. If not, please describe how its obsolescence will be communicated to users.)

Versioning of the dataset is managed via DaRUS. Data can only be added. For additional information see <https://guides.dataverse.org/en/5.9/user/dataset-management.html#dataset-versions>

7. If others want to extend/augment/build on/contribute to the dataset, is there a mechanism for them to do so? (If so, please provide a description. Will these contributions be validated/verified? If so, please describe how. If not, why not? Is there a process for communicating/distributing these contributions to other users? If so, please provide a description.)

Errors may be submitted via the bugtracker on github.

8. Any other comments?

None.

K.8 Reproducibility of the baseline score

We provide all the pretrained model in our DaRUS repository: <https://darus.uni-stuttgart.de/privateurl.xhtml?token=cd862f8c-8e1b-49d2-b4da-b35f8df5ac85>. So users can freely check our result or even continue longer training with the help of our APIs.

K.9 Reading and using the dataset

The downloaded HDF5 files can easily be read by a standard software to read HDF5 files. Concerning the data size, 1D data have 4 - 20 GB, 2D data have 6 - 100 GB, 3D data have 60 - 80 GB, depending on PDEs and parameters. In our project home page <https://github.com/pdebench/PDEBench/blob/main/README.md>, we also provide APIs to read and store the data into PyTorch data loader, which could be directly used in the user's code or our providing ML model training APIs.

An example of snipped code for reading data is introduced in subsection 3.5. Information on how to use the baseline and read the dataset is provided in the project home page.

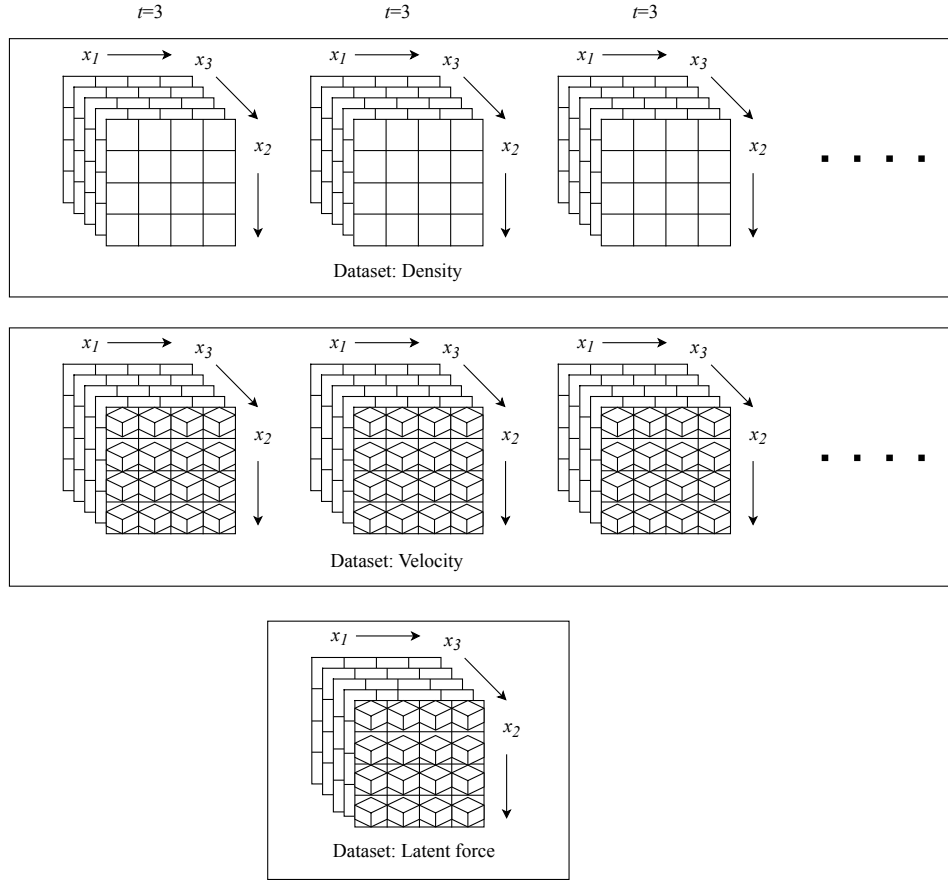


Figure 34: Example of data format for a PDE with density and velocity terms

K.10 Data Format

Fig.34 visualizes the data format of PDEBENCH.

Realizations are stored in HDF5 format, allowing typed storage of dense arrays on disk. File naming format is $\{\text{PDE name}\}--\{\text{Parameters}\}--\{\text{Config}\}.h5$. The HDF file contains a single group, documented in the source code for the generating PDE, which may contain multiple HDF5 datasets, corresponding to tensors.

Arrays are packed according to the convention $(b \times t \times x_1 \cdots \times x_d \times v)$, where b denotes the samples' dimension, t the time dimension, x_1, \dots, x_d the d spatial dimensions, and v the dimensions needed to encode the state of the system (e.g. a scalar density field has dimension one, a 2d velocity field might have dimension 2)¹¹. Not all dimensions are present in all data sets; for example, some parameters are be time-invariant, in which case the time dimension does not exist. For each file, simulation parameters are stored alongside the simulation runs as HDF5 attribute strings in YAML format encoded as UTF8.

¹¹ Concerning the compressible Navier-Stokes equations' dataset, each variable is provided independently, not summarized into a channel dimension (i.e. extending the array by 1 dimension), such as "density" and "pressure". This is to avoid too big array sizes, allowing memory efficient data I/O by sub-sampling spatial cells.